

This is an Open Access document downloaded from ORCA, Cardiff University's institutional repository: <https://orca.cardiff.ac.uk/id/eprint/147326/>

This is the author's version of a work that was submitted to / accepted for publication.

Citation for final published version:

Ai, Congfang, Ma, Yuxiang, Ding, Weiye, Xie, Zhihua and Dong, Guohai 2022. Three-dimensional non-hydrostatic model for dam-break flows. *Physics of Fluids* 34 (2) , 022105. 10.1063/5.0081094

Publishers page: <http://dx.doi.org/10.1063/5.0081094>

Please note:

Changes made as a result of publishing processes such as copy-editing, formatting and page numbers may not be reflected in this version. For the definitive version of this publication, please refer to the published source. You are advised to consult the publisher's version if you wish to cite this paper.



This version is being made available in accordance with publisher policies. See <http://orca.cf.ac.uk/policies.html> for usage policies. Copyright and moral rights for publications made available in ORCA are retained by the copyright holders.



Three-dimensional non-hydrostatic model for dam-break flows

Cite as: Phys. Fluids **34**, 022105 (2022); <https://doi.org/10.1063/5.0081094>

Submitted: 06 December 2021 • Accepted: 21 January 2022 • Published Online: 08 February 2022

Congfang Ai (艾丛芳),  Yuxiang Ma (马玉祥),  Weiye Ding (丁伟业), et al.



View Online



Export Citation



CrossMark

ARTICLES YOU MAY BE INTERESTED IN

[Numerical investigation of flow structure and air entrainment of breaking bow wave generated by a rectangular plate](#)

Physics of Fluids **33**, 122113 (2021); <https://doi.org/10.1063/5.0077348>

[Rescaling the near-wall predictive model for passive scalars in turbulent channel flow](#)

Physics of Fluids **34**, 021704 (2022); <https://doi.org/10.1063/5.0080962>

[A phase-field-based lattice Boltzmann model for multiphase flows involving N immiscible incompressible fluids](#)

Physics of Fluids **34**, 023311 (2022); <https://doi.org/10.1063/5.0078507>



Author Services

English Language Editing

High-quality assistance from subject specialists

LEARN MORE



Three-dimensional non-hydrostatic model for dam-break flows

Cite as: Phys. Fluids **34**, 022105 (2022); doi: [10.1063/5.0081094](https://doi.org/10.1063/5.0081094)

Submitted: 6 December 2021 · Accepted: 21 January 2022 ·

Published Online: 8 February 2022



View Online



Export Citation



CrossMark

Congfang Ai (艾丛芳),¹ Yuxiang Ma (马玉祥),^{1,a)}  Weiye Ding (丁伟业),²  Zhihua Xie (谢志华),³ 
and Guohai Dong (董国海)¹

AFFILIATIONS

¹State Key Laboratory of Coastal and Offshore Engineering, Dalian University of Technology, 116024 Dalian, China

²School of Marine Engineering Equipment, Zhejiang Ocean University, 316022 Zhoushan, China

³Hydro-environmental Research Centre, School of Engineering, Cardiff University, CF10 3AT Cardiff, United Kingdom

^{a)} Author to whom correspondence should be addressed: yuxma@dlut.edu.cn

ABSTRACT

A three-dimensional (3D) non-hydrostatic model is presented for the simulation of dam-break flows. The model solves the Reynolds-averaged Navier–Stokes equations using the projection method. 3D computational grids are constructed from a two-dimensional horizontal unstructured mesh by adding horizontal layers in the vertical direction. Based on the horizontal unstructured grid system, horizontal advection terms are discretized by a momentum conservative scheme. The proposed model is validated with several physical experiments. The agreement between the model results and experimental data is generally good, which demonstrates the capability of the proposed model to resolve dam-break flows over flat and uneven bottoms with complex geometries. Moreover, the efficiency of the model is evaluated with 3D dam-break flow experiments. Comparisons between the non-hydrostatic model and the corresponding quasi-3D shallow water model are also performed, which confirm the role of non-hydrostatic effects in dam-break flows.

Published under an exclusive license by AIP Publishing. <https://doi.org/10.1063/5.0081094>

I. INTRODUCTION

It is very important to investigate and predict dam-break flows, because they can cause catastrophic damage to public facilities and private property. Many physical experiments have been carried out in the past to study dam-break processes (Fraccarollo and Toro, 1995; Khankandi *et al.*, 2012; LaRocque *et al.*, 2013; and Mohapatra and Chaudhry, 2004) and dam-break flows against uneven bottoms or complex geometries (Aureli *et al.*, 2008; Kocaman and Ozmen-Cagatay, 2012; O'Donoghue *et al.*, 2010; Ozmen-Cagatay and Kocaman, 2011; Soares-Fraão, 2007; and Testa *et al.*, 2007). Along with experimental studies, efforts have been focused on establishing numerical models in the hope that more and accurate details of dam-break flows can be obtained. Numerical models for dam-break flows can be classified into two categories depending on whether the hydrostatic pressure distribution is assumed. The first is a class of models incorporating the hydrostatic pressure distribution. One of the most famous of such models is the classical two-dimensional (2D) shallow water equations model (SWM). The other class of models incorporates non-hydrostatic effects and has the capability of predicting dispersive waves. Over the past three decades, a large number of 2D SWMs (Brufau *et al.*, 2002; Chang *et al.*, 2011; Fyhn *et al.*, 2019; Lai *et al.*,

2005; Mingham and Causon, 1998; Ortiz, 2014; Zhao *et al.*, 2021; and Zhao *et al.*, 1994) have been developed to examine dam-break flows. It is generally believed that numerical models with the assumption of hydrostatic pressure are capable of satisfactorily predicting dam-break flows and their interaction with uneven bottoms or complex geometries. However, it has been demonstrated by some previous studies (Biscarini *et al.*, 2010; Cantero-Chinchilla *et al.*, 2016; Ferrari *et al.*, 2010; Kim and Lynett, 2011; Ozmen-Cagatay and Kocaman, 2011; and Stansby *et al.*, 1998) that numerical models incorporating non-hydrostatic effects work better than 2D SWMs in some dam-break flows. Therefore, to accurately predict dam-break flows, numerical models incorporating non-hydrostatic effects have attracted increasing attention.

The Boussinesq-type model is an option for the non-hydrostatic simulation of dam-break flows. The model can be viewed as an extension of SWM by including an additional correction term to account for non-hydrostatic effects. Similar to 2D SWMs, Boussinesq-type models are usually depth-averaged and are thus computationally efficient with the trade-off of losing depth-related information. Many Boussinesq-type models (Cantero-Chinchilla *et al.*, 2016; Chang *et al.*, 2014; Kim and Lynett, 2011; Mignot and Cienfuegos, 2009; and

Mohapatra and Chaudhry, 2004) have been successfully applied to simulate dam-break flows. For example, Kim and Lynett (2011) employed a 2D Boussinesq-type equations model to simulate a 1D dam-break experiment and dam-break flows against an L -shaped channel (Soares-Frazão and Zech, 2002). It was found that the model captures undular bores in two dam-break tests, which may be attributed to the weakly non-hydrostatic pressure assumption incorporated in the model. Mohapatra and Chaudhry (2004) utilized a fourth-order explicit numerical procedure to solve the one-dimensional (1D) Boussinesq equations for the simulation of dam-break flows. Their results showed that the water surface profiles of different depth ratios have undulations near the bore front for depth ratios greater than 0.4.

In addition to Boussinesq-type models, numerical models based on the Navier–Stokes equations (NSE) are also capable of predicting non-hydrostatic effects in dam-break flows. NSE models allow vertical variations in the velocity and pressure distribution and thus may work better than depth-averaged Boussinesq-type models, because both the computed and measured horizontal velocity profiles obtained from idealized dam-break flows indicated that a shear layer is in the near-bed velocity profiles (LaRocque *et al.*, 2013). However, solving NSE models usually requires more computational effort, which is due to the following two reasons. The first is that the NSE models have to solve the Poisson equation, which is computationally expensive. The second is that NSE models usually require more computational effort to numerically capture the moving free surface. The treatment of the free surface is one of the difficulties in developing NSE-based models. Many methods have been used to simulate this moving boundary, such as the volume of fluid (VOF) method (Hirt and Nichols, 1981), the level-set method (Osher and Sethian, 1988), the coupled level-set/volume-of-fluid (CLSVOF) method (Duy *et al.*, 2021; Li *et al.*, 2020; and Ling *et al.*, 2019), and the tangent of hyperbolic interface capturing (THINC) method (Li *et al.*, 2014 and Xie and Xiao, 2017). Many VOF-based NSE models (Biscarini *et al.*, 2010; Marsooli and Wu, 2014; Ozmen-Cagatay and Kocaman, 2011; and Xie *et al.*, 2021) have been developed and successfully applied to simulate dam-break flows. These models can deal with complicated free surfaces (e.g., overturning flows), but their application is limited by high computational expenses. To improve computational efficiency, Mintgen and Manhart (2018) presented a coupled model between a 2D SWM and a VOF-based NSE model.

To efficiently track the free surface, the so-called free surface equation can be used in NSE-based models. This equation is obtained by integrating the continuity equation over the water depth and applying Leibniz's rule with kinematic boundary conditions at the impermeable bottom and the moving free surface. By discarding depth-related information, the free-surface equation is converted to the mass conservation equation employed by 2D SWMs or Boussinesq-type models. Non-hydrostatic models are developed based upon NSE but employ the free-surface equation to capture the moving free surface. In contrast to VOF-based NSE models (Biscarini *et al.*, 2010; Marsooli and Wu, 2014; Munoz and Constantinescu, 2020; Ozmen-Cagatay and Kocaman, 2011; and Xie *et al.*, 2021), non-hydrostatic models cannot simulate overturning flows, but they can predict free-surface flows with a relatively coarse vertical discretization, in which the free surface is defined as a single-valued function of the horizontal plane. Therefore, non-hydrostatic models can be more computationally efficient than VOF-based NSE models.

Three-dimensional (3D) non-hydrostatic models are relative to 3D hydrostatic models, which solve the NSE with the hydrostatic pressure assumption and are usually referred to as quasi-3D SWMs (Lu *et al.*, 2020). Quasi-3D SWMs can provide 3D flow patterns with affordable computational expense and are widely applied in river, estuarine, and ocean flow simulations. However, they cannot predict flows involving non-hydrostatic effects. The development of non-hydrostatic models has evolved for more than twenty years. To date, non-hydrostatic models have been widely used in predictions of short surface waves (Ai *et al.*, 2011; Ai *et al.*, 2019a; Ma *et al.*, 2012; Wu *et al.*, 2010; Young *et al.*, 2009; and Zijlema and Stelling, 2005), internal waves (Ai and Ding, 2016; Ai *et al.*, 2021, 2021b; Lai *et al.*, 2010; and Vasarmidis *et al.*, 2019), tsunami waves (Ai *et al.*, 2021a, 2021b; Oishi *et al.*, 2013; and Pan *et al.*, 2020), and even wave-structure interactions (Ai and Jin, 2010; Ai *et al.*, 2019b; Ma *et al.*, 2019; Ma *et al.*, 2016; and Rijnssdorp and Zijlema, 2016). In addition, Bristeau *et al.* (2011) presented a two-dimensional vertical non-hydrostatic Saint-Venant model and used it to simulate a dam-break flow over a bump. Aricò and Re (2016) proposed a 2D depth-integrated non-hydrostatic model that successfully simulated partial dam-break flows. However, to the best of our knowledge, no papers on the simulation of dam-break flows with 3D non-hydrostatic models that use the free-surface equation to capture the moving free surface have been published.

In this paper, we will extend our non-hydrostatic model (Ai and Jin, 2010) to simulate dam-break flows and validate the developed model for a wide range of test cases. The previous non-hydrostatic model (Ai and Jin, 2010) utilizes the projection method to solve the NSE, but it only employs the Smagorinsky model (Smagorinsky, 1963) to calculate eddy viscosities. Moreover, the horizontal layers are distributed following a z -coordinate system in the vertical direction. The extension of the previous model is conducted by incorporating a boundary-fitted coordinate system in the vertical direction and employing the Smagorinsky model (Smagorinsky, 1963) and the standard $k - \varepsilon$ model (Rodi, 1984) to calculate the horizontal eddy viscosity and the vertical eddy viscosity, respectively. The 3D grid system is built from a two-dimensional horizontal unstructured mesh by adding horizontal layers. The developed model is validated using five test cases, including 2D and 3D dam-break flows over flat and uneven bottoms with complex geometries. The efficiency of the model is demonstrated through 3D dam-break flow experiments. The developed non-hydrostatic model results are also compared with the corresponding quasi-3D SWM results to show the importance of non-hydrostatic effects in dam-break flows.

The remainder of this paper is organized as follows. In Sec. II, the mathematical formulation together with boundary conditions is presented. In Sec. III, the numerical methods used to solve the non-hydrostatic model are described. Validation results are presented in Sec. IV, and conclusions are provided in Sec. V.

II. MATHEMATICAL FORMULATION

A. Governing equations and boundary conditions

The non-hydrostatic model employs the incompressible Reynolds-averaged Navier–Stokes (RANS) equations as governing equations. By splitting the pressure into hydrostatic and non-hydrostatic ones, $p = g(\eta - z) + q$, they can be expressed in the following form:

$$\frac{\partial u}{\partial x} + \frac{\partial v}{\partial y} + \frac{\partial w}{\partial z} = 0, \quad (1)$$

$$\frac{\partial u}{\partial t} + \frac{\partial u^2}{\partial x} + \frac{\partial uv}{\partial y} + \frac{\partial uw}{\partial z} = -g \frac{\partial \eta}{\partial x} - \frac{\partial q}{\partial x} + \nu^h \left(\frac{\partial^2 u}{\partial x^2} + \frac{\partial^2 u}{\partial y^2} \right) + \nu^v \left(\frac{\partial^2 u}{\partial z^2} \right), \quad (2)$$

$$\frac{\partial v}{\partial t} + \frac{\partial uv}{\partial x} + \frac{\partial v^2}{\partial y} + \frac{\partial vw}{\partial z} = -g \frac{\partial \eta}{\partial y} - \frac{\partial q}{\partial y} + \nu^h \left(\frac{\partial^2 v}{\partial x^2} + \frac{\partial^2 v}{\partial y^2} \right) + \nu^v \left(\frac{\partial^2 v}{\partial z^2} \right), \quad (3)$$

$$\frac{\partial w}{\partial t} + \frac{\partial uw}{\partial x} + \frac{\partial vw}{\partial y} + \frac{\partial w^2}{\partial z} = -\frac{\partial q}{\partial z} + \nu^h \left(\frac{\partial^2 w}{\partial x^2} + \frac{\partial^2 w}{\partial y^2} \right) + \nu^v \left(\frac{\partial^2 w}{\partial z^2} \right), \quad (4)$$

where u , v , and w are the velocity components in the horizontal x , y , and vertical z directions, respectively; t is the time; p is the normalized pressure divided by a constant reference density; η is the free surface elevation; q is the non-hydrostatic pressure component; g is the gravitational acceleration; and ν^h and ν^v are the horizontal and vertical eddy viscosities, respectively. To consider the difference between horizontal and vertical grid resolutions, the horizontal eddy viscosity ν^h is determined by the Smagorinsky model (Smagorinsky, 1963), and the vertical eddy viscosity ν^v is evaluated with the standard $k-\varepsilon$ model (Rodi, 1984).

The free-surface elevation η is determined by the following free-surface equation, which can be derived from the vertical integration of the continuity equation (1) plus kinematic boundary conditions at the impermeable bottom and the moving free surface,

$$\frac{\partial \eta}{\partial t} + \frac{\partial}{\partial x} \int_{-d}^{\eta} u dz + \frac{\partial}{\partial y} \int_{-d}^{\eta} v dz = 0, \quad (5)$$

where $z = -d(x, y)$ is the bottom surface.

At the free surface, the zero pressure boundary condition should be imposed because the atmospheric pressure is exerted there. On the impermeable bottom $z = -d(x, y)$, the bottom friction is specified by

$$\frac{\tau_{0x}}{\rho} = \nu^v \frac{\partial u}{\partial z} = \gamma_b u_1, \quad \frac{\tau_{0y}}{\rho} = \nu^v \frac{\partial v}{\partial z} = \gamma_b v_1, \quad (6)$$

where τ_{0x} and τ_{0y} are the shear stress components in the directions x and y , respectively; u_1 and v_1 are the velocities at the bottom cell; $\gamma_b = c_f \sqrt{u_1^2 + v_1^2} / h$, where $h = \eta + d$ is the water depth; c_f is the dimensionless friction coefficient and is determined from the Manning-Strickler formula as $c_f = 0.015(k_s/h)^{1/3}$, where k_s is a roughness value and needs to be calibrated.

Finally, at the inflow boundary, velocities normal to the boundary are specified based on the laboratory measurement of incoming flows. At the outflow boundary, an open boundary condition is imposed using a zero gradient condition for the outlet velocities.

B. Governing equations in the vertical boundary-fitted coordinate system

The presented model solves the governing equations in a vertical boundary-fitted coordinate system, which automatically fits the bed and free surface and is illustrated in Fig. 1. In Fig. 1, the physical domain is divided into N_z horizontal layers in the vertical direction.

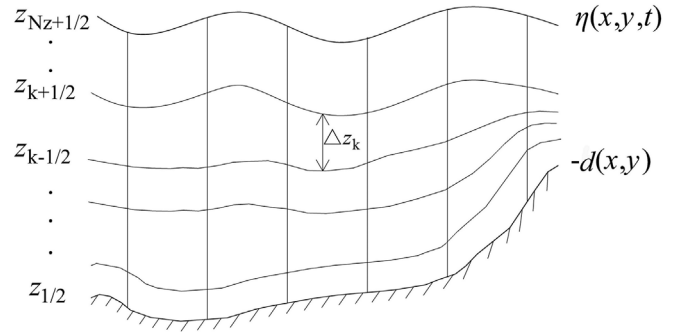


FIG. 1. Schematic sketch of the vertical boundary-fitted coordinate system.

The interface between two layers is defined as $z_{k+1/2}(x, y, t)$, and uniformly distributed layers are employed in this study, so that $z_{k+1/2}(x, y, t)$ is computed as follows:

$$z_{k+1/2}(x, y, t) = d(x, y) + k \cdot h(x, y, t) / N_z, \quad (7)$$

where k is a layer index.

Notably, the layer level $z_{k+1/2}(x, y, t)$ varies with time, so the employed boundary-fitted coordinate system is a moving grid system. In such vertical grid systems, Eqs. (1)–(4) can be transformed into the following equations by integrating them over a vertical layer bounded by $z_{k-1/2}(x, y, t)$ and $z_{k+1/2}(x, y, t)$:

$$\frac{\partial \Delta z_k}{\partial t} + \frac{\partial (\Delta z u)_k}{\partial x} + \frac{\partial (\Delta z v)_k}{\partial y} + \omega_{k+1/2} - \omega_{k-1/2} = 0, \quad (8)$$

$$\begin{aligned} \frac{\partial (\Delta z u)_k}{\partial t} + \frac{\partial (\Delta z u u)_k}{\partial x} + \frac{\partial (\Delta z u v)_k}{\partial y} + \omega_{k+1/2} u_{k+1/2} - \omega_{k-1/2} u_{k-1/2} \\ = -g \Delta z_k \frac{\partial \eta}{\partial x} - \Delta z_k \frac{\partial q}{\partial x} + \Delta z_k (F_u)_k, \end{aligned} \quad (9)$$

$$\begin{aligned} \frac{\partial (\Delta z v)_k}{\partial t} + \frac{\partial (\Delta z u v)_k}{\partial x} + \frac{\partial (\Delta z v v)_k}{\partial y} + \omega_{k+1/2} v_{k+1/2} - \omega_{k-1/2} v_{k-1/2} \\ = -g \Delta z_k \frac{\partial \eta}{\partial y} - \Delta z_k \frac{\partial q}{\partial y} + \Delta z_k (F_v)_k, \end{aligned} \quad (10)$$

$$\begin{aligned} \frac{\partial (\Delta z w)_k}{\partial t} + \frac{\partial (\Delta z u w)_k}{\partial x} + \frac{\partial (\Delta z v w)_k}{\partial y} + \omega_{k+1/2} w_{k+1/2} - \omega_{k-1/2} w_{k-1/2} \\ = -\Delta z_k \frac{\partial q}{\partial z} + \Delta z_k (F_w)_k, \end{aligned} \quad (11)$$

where $\Delta z_k = z_{k+1/2} - z_{k-1/2}$; F_u , F_v , and F_w represent the momentum diffusion terms; and $\omega_{k+1/2}$ is the vertical velocity relative to the layer level $z_{k+1/2}$. Noting that $\omega_{1/2} = \omega_{N_z+1/2} = 0$.

For the sake of brevity, details about the transformation are not presented here and can instead be found in Ai et al. (2011) and Zijlema and Stelling (2005).

III. NUMERICAL APPROXIMATIONS

A. 3D grid system

Before discretizing the governing equations, the computational domain is covered by a 3D grid system, which is built from a two-dimensional horizontal triangular mesh by simply adding some horizontal layers. Thus, the grid system is composed of many prisms.

Figure 2 shows the definition of variables, in which i is the index of a horizontal triangular grid and the sides of the i th triangle are identified by an index $j(i, l)$, $l = 1, 2, 3$. In the horizontal triangular grids, λ_j is the length of the j th side and δ_j is the distance between the circumcenters of two adjacent triangles, which share the j th side.

As illustrated in Fig. 2, the variables are defined as follows. The free surface elevation is located at the circumcenter of a triangle; the horizontal velocity component normal to each face of a prism is defined at the point of intersection between the face and the segment joining the centers of the two neighboring prisms. The vertical velocity component is defined at the center of a prism. Finally, the non-hydrostatic pressure and vertical relative velocity are located at the circumcenter of the i th triangle and the layer level.

B. Treatment of time derivative terms

Considering the definition of the horizontal velocity component and the invariant property of Eqs. (9)–(11) under solid rotation of the x and y axes around the z axis, the horizontal momentum equation we need to solve can be expressed as

$$\begin{aligned} \frac{\partial(\Delta zu)_{j,k}}{\partial t} + \frac{\partial(\Delta zuu)_{j,k}}{\partial \xi} + \frac{\partial(\Delta zuv)_{j,k}}{\partial \zeta} \\ + \omega_{j,k+1/2} u_{j,k+1/2} - \omega_{j,k-1/2} u_{j,k-1/2} \\ = -g \Delta z_{j,k} \left(\frac{\partial \eta}{\partial \xi} \right)_{j,k} - \Delta z_{j,k} \left(\frac{\partial q}{\partial \xi} \right)_{j,k} + \Delta z_{j,k} (F_u)_{j,k}, \end{aligned} \quad (12)$$

where $u_{j,k}$ is the horizontal velocity component normal to the face of a prism; ξ is the normal direction defined on the j th side; and ζ is the counterclockwise orthogonal direction of ξ .

Following Kramer and Stelling (2008), the time derivative in Eq. (12) can be split into following two terms:

$$\frac{\partial(\Delta zu)_{j,k}}{\partial t} = \Delta z_{j,k} \frac{\partial u_{j,k}}{\partial t} + u_{j,k} \frac{\partial \Delta z_{j,k}}{\partial t}. \quad (13)$$

By substituting Eq. (8) into Eq. (13), we can obtain

$$\begin{aligned} \frac{\partial(\Delta zu)_{j,k}}{\partial t} = \Delta z_{j,k} \frac{\partial u_{j,k}}{\partial t} - u_{j,k} \left[\frac{\partial(\Delta zu)_k}{\partial x} + \frac{\partial(\Delta zv)_k}{\partial y} \right] \\ - u_{j,k} (\omega_{k+1/2} - \omega_{k-1/2}). \end{aligned} \quad (14)$$

Then, by further substituting Eq. (14) into Eq. (12), after which it is divided by $\Delta z_{j,k}$ yields

$$\frac{\partial u_{j,k}}{\partial t} + AdvH(u_{j,k}) + AdvV(u_{j,k}) = -g \left(\frac{\partial \eta}{\partial \xi} \right)_{j,k} - \left(\frac{\partial q}{\partial \xi} \right)_{j,k} + (F_u)_{j,k}, \quad (15)$$

where

$$\begin{aligned} AdvH(u_{j,k}) = \frac{1}{\Delta z_{j,k}} \left[\frac{\partial(\Delta zuu)_{j,k}}{\partial \xi} + \frac{\partial(\Delta zuv)_{j,k}}{\partial \zeta} \right] \\ - \frac{u_{j,k}}{\Delta z_{j,k}} \left[\frac{\partial(\Delta zu)_k}{\partial \xi} + \frac{\partial(\Delta zv)_k}{\partial \zeta} \right] \end{aligned} \quad (16)$$

and

$$\begin{aligned} AdvV(u_{j,k}) = \frac{1}{\Delta z_{j,k}} (\omega_{j,k+1/2} u_{j,k+1/2} - \omega_{j,k-1/2} u_{j,k-1/2}) \\ - \frac{u_{j,k}}{\Delta z_{j,k}} (\omega_{k+1/2} - \omega_{k-1/2}). \end{aligned} \quad (17)$$

We also apply the above procedure to treat the time derivative in Eq. (11) and obtain the following expression for $w_{i,k}$:

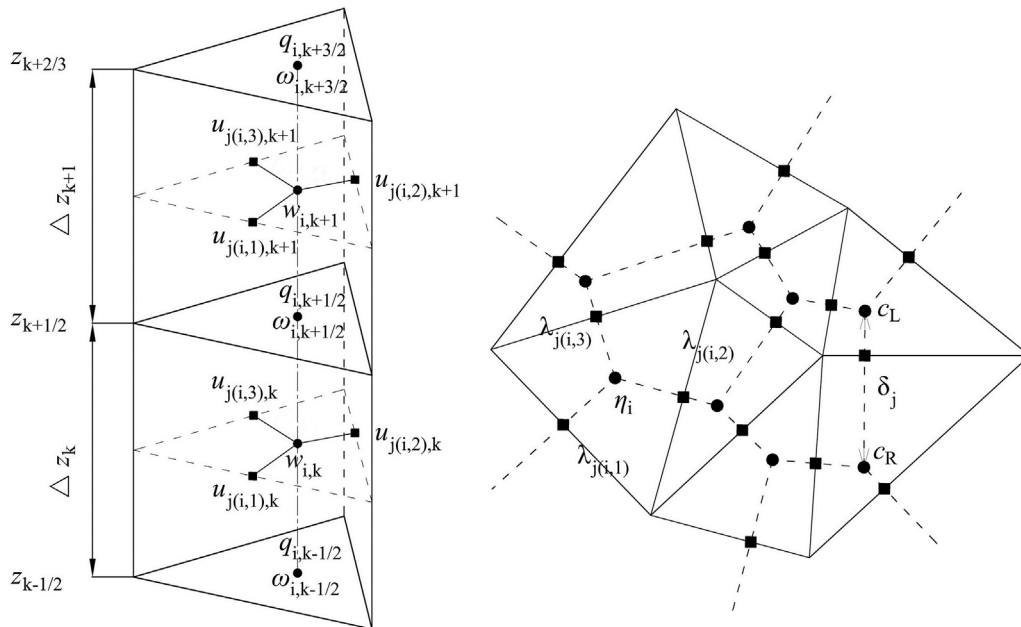


FIG. 2. Definition sketch of variables.

$$\frac{\partial w_{i,k}}{\partial t} + AdvH(w_{i,k}) + AdvV(w_{i,k}) = -\left(\frac{\partial q}{\partial z}\right)_{i,k} + (F_w)_{i,k}, \quad (18)$$

where

$$AdvH(w_{i,k}) = \frac{1}{\Delta z_{i,k}} \left[\frac{\partial(\Delta zuw)_{i,k}}{\partial x} + \frac{\partial(\Delta zvw)_{i,k}}{\partial y} \right] - \frac{w_{i,k}}{\Delta z_{i,k}} \left[\frac{\partial(\Delta zu)_{i,k}}{\partial x} + \frac{\partial(\Delta zv)_{i,k}}{\partial y} \right] \quad (19)$$

and

$$AdvV(w_{i,k}) = \frac{\omega_{i,k-1/2}}{\Delta z_{i,k}} (w_{i,k+1/2} - w_{i,k}) - \frac{\omega_{i,k-1/2}}{\Delta z_{i,k}} (w_{i,k-1/2} - w_{i,k}). \quad (20)$$

C. The projection method

An explicit projection method is applied to solve the governing equations (1), (15), and (18), which is described as follows.

First, we solve Eqs. (15) and (18) by neglecting the contribution of the non-hydrostatic pressure to explicitly compute provisional values $u_{j,k}^*$ and $w_{i,k}^*$. This gives

$$\frac{u_{j,k}^* - u_{j,k}^n}{\Delta t} + AdvH(u_{j,k}^n) + AdvV(u_{j,k}^n) = -g \left(\frac{\partial \eta}{\partial \xi} \right)_{j,k}^n + (F_u)_{j,k}^n, \quad (21)$$

$$\frac{w_{i,k}^* - w_{i,k}^n}{\Delta t} + AdvH(w_{i,k}^n) + AdvV(w_{i,k}^n) = (F_w)_{i,k}^n, \quad (22)$$

where Δt is the time step.

Second, the provisional values $u_{j,k}^*$ and $w_{i,k}^*$ can be corrected with

$$\frac{u_{j,k}^{n+1} - u_{j,k}^*}{\Delta t} = -\left(\frac{\partial q}{\partial \xi}\right)_{j,k}^{n+1}, \quad (23)$$

$$\frac{w_{i,k}^{n+1} - w_{i,k}^*}{\Delta t} = -\left(\frac{\partial q}{\partial z}\right)_{i,k}^{n+1}. \quad (24)$$

The water surface gradient term in Eq. (21) and the non-hydrostatic pressure gradient terms in Eqs. (23) and (24) can be easily discretized by the central difference scheme. Before computing the final values $u_{j,k}^{n+1}$ and $w_{i,k}^{n+1}$, non-hydrostatic pressures must be determined by the Poisson equation, which can be obtained as follows.

Equation (1) can be discretized by a combination of finite difference and finite volume methods. This gives the following:

For $k = 2, \dots, N_z$

$$\frac{1}{P_i} \sum_{l=1}^3 s_{i,l} \lambda_{j(i,l)} u_{j(i,l),k-1/2}^{n+1} + \frac{w_{i,k}^{n+1} - w_{i,k-1}^{n+1}}{\Delta z_{i,k-1/2}} = 0, \quad (25)$$

where $u_{j(i,l),k-1/2}^{n+1} = [u_{j(i,l),k}^{n+1} + u_{j(i,l),k-1}^{n+1}] / 2$; P_i is the area of the i th element; and $s_{i,l}$ is a sign function associated with the orientation of the normal velocity defined on the l th side of the i th element. Assuming a positive velocity on the l th side, $s_{i,l} = 1$ corresponds to outflow from the i th element, and $s_{i,l} = -1$ corresponds to inflow into the i th element.

For $k = 1$, Eq. (1) is discretized in a half bottom layer. Considering $w_{i,1/2}^{n+1} = 0$, we can obtain the following expression:

$$\frac{1}{P_i} \sum_{l=1}^3 s_{i,l} \lambda_{j(i,l)} u_{j(i,l),1}^{n+1} + \frac{w_{i,1}^{n+1}}{\Delta z_{i,1}^{n+1}/2} = 0. \quad (26)$$

Substituting Eqs. (23) and (24) into Eqs. (25) and (26), we obtain the Poisson equation, which can be written in the following matrix form:

$$\mathbf{A} \mathbf{q} = \mathbf{b}, \quad (27)$$

where \mathbf{A} is a sparse coefficient matrix; \mathbf{q} is a vector of the calculated non-hydrostatic pressure; and \mathbf{b} is a known vector related to the provisional velocities. Equation (27) is a symmetric and positive definite system. Thus, it can be efficiently solved by the preconditioned conjugate gradient method. Moreover, it contains 8 nonzero diagonals for the bottom layer and 12 nonzero diagonals for other layers.

D. Discretization of advection terms

As illustrated in Fig. 2, the variables are defined at staggered locations in the horizontal plane. Therefore, we can employ Perot's scheme (Perot, 2000) to achieve a momentum conservation advection scheme. Following Perot's scheme, the horizontal advection term $AdvH(u_{j,k})$ in Eq. (15) can be calculated as follows:

$$AdvH(u_{j,k}^n) = \alpha_{c_L} AdvH(\mathbf{U}_{c_L,k}^n) \cdot \mathbf{n}_j + \alpha_{c_R} AdvH(\mathbf{U}_{c_R,k}^n) \cdot \mathbf{n}_j, \quad (28)$$

where \mathbf{n}_j is the normal vector defined at the j th side; c_L and c_R are the indices of two adjacent triangles, which share the j th side (see Fig. 2); $\mathbf{U}_{c_L,k}^n$ and $\mathbf{U}_{c_R,k}^n$ denote horizontal velocity vectors stored at triangles c_L and c_R , respectively; and α_{c_L} and α_{c_R} are the weighting factors of the j th side and can be determined as follows:

$$\alpha_{c_L} = \frac{\Delta \delta_{c_L,j}}{\delta_j}, \quad \alpha_{c_R} = \frac{\Delta \delta_{c_R,j}}{\delta_j}, \quad (29)$$

where $\Delta \delta_{c_L,j}$ and $\Delta \delta_{c_R,j}$ are the distances from the circumcenters of triangles c_L and c_R to the center of the j th side, respectively, and thus $\Delta \delta_{c_L,j} + \Delta \delta_{c_R,j} = \delta_j$.

The horizontal advection vectors $AdvH(\mathbf{U}_{c_L,k}^n)$ and $AdvH(\mathbf{U}_{c_R,k}^n)$ are defined at triangles c_L and c_R , respectively. Without loss of generality, for $AdvH(\mathbf{U}_{i,k}^n)$ which is defined at the i th element and k th layer, it can be expressed in the following finite volume form:

$$AdvH(\mathbf{U}_{i,k}^n) = \frac{1}{P_i \Delta z_{i,k}} \sum_{l=1}^3 s_{i,l} \lambda_{j(i,l)} \Delta z_{j(i,l),k}^n \hat{\mathbf{U}}_{j(i,l),k}^n, \quad (30)$$

where $\hat{\mathbf{U}}_{j(i,l),k}^n$ denotes the horizontal velocity vector on side $j(i,l)$ of the i th element, which is determined by the upwind method in this study.

For the vertical momentum equation (18), its horizontal advection term $AdvH(w_{i,k})$ can be discretized following Eq. (30) by means of the finite volume method. The vertical advection terms $AdvV(u_{j,k})$ in Eq. (15) and $AdvV(w_{i,k})$ in Eq. (18) can be discretized directly by using the finite difference method because the 3D grid system is structured in the vertical direction. The horizontal part of the diffusion term $(F_u)_{j,k}$ in Eq. (15) is also discretized by Perot's scheme following Eq. (28), while the horizontal part of the diffusion term $(F_w)_{i,k}$ in Eq. (18) can be directly discretized by the finite volume method. The vertical parts of the diffusion term $(F_u)_{j,k}$ in Eq. (15) and the diffusion

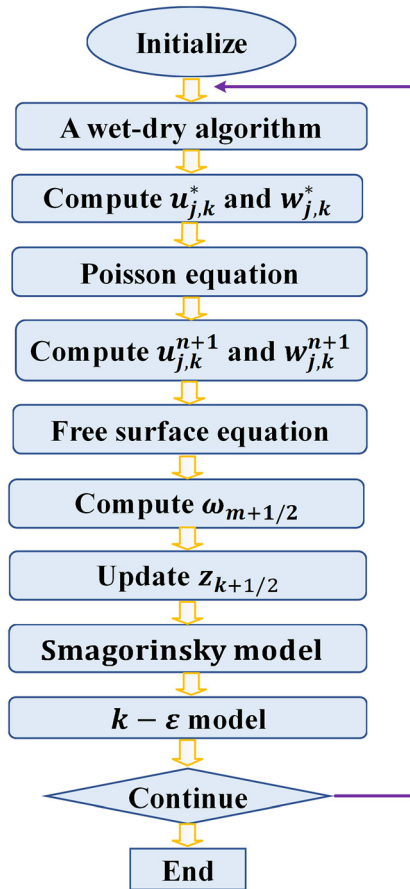


FIG. 3. Flow chart for the overall solution procedure.

term $(F_w)_{i,k}$ in Eq. (18) are discretized by the finite difference method. For the sake of brevity, all of the details are not given here and can be found in Ai and Jin (2010).

E. Solution procedure

Figure 3 shows the flow chart for the overall solution procedure, which is summarized as follows.

- (1) Configure the 3D grid system and the initial values of the variables at the initialization step.
- (2) Implement the wet–dry algorithm proposed by Ai and Jin (2012) to describe the wet–dry fronts.
- (3) Obtain the provisional velocities $u_{j,k}^*$ and $w_{i,k}^*$ by solving Eqs. (21) and (22), respectively.
- (4) Solve Poisson equation (27) by using the conjugate gradient method with a symmetric Gauss–Seidel preconditioner. If wave breaking occurs, a wave breaking algorithm should be incorporated before Poisson equation (27) is solved.
- (5) Update the provisional velocities using Eqs. (23) and (24) to obtain the new velocities $u_{j,k}^{n+1}$ and $w_{i,k}^{n+1}$, respectively.
- (6) Calculate the new water surface elevation η_i^{n+1} by applying a finite volume discretization to solve Eq. (5).
- (7) Calculate the new relative velocity $\omega_{k+1/2}^{n+1}$ by also applying a finite volume discretization to solve Eq. (8). Note that $\omega_{1/2}^{n+1} = \omega_{N_z+1/2}^{n+1} = 0$.
- (8) Update the layer level $z_{k+1/2}(x, y, t)$ using Eq. (7).
- (9) Compute the horizontal eddy viscosities by solving the Smagorinsky model (Smagorinsky, 1963).
- (10) Compute the vertical eddy viscosities by solving the standard $k - \epsilon$ model (Rodi, 1984). The standard $k - \epsilon$ model is discretized by a combination of finite difference and finite volume methods following Eq. (18).

In addition, a quasi-3D SWM can be obtained by neglecting the Poisson equation (27) and employing a semi-implicit method (Casulli and Zanolli, 2002) to discretize the water surface gradient in Eq. (15). In the quasi-3D SWM, the implicitness factor is set to $\theta = 0.5$ for the sake of stability.

IV. MODEL VALIDATIONS

In this section, five test cases are employed to verify the capability of the non-hydrostatic model for handling dam-break flows. The first two test cases concern 2D dam-break flows, while the last three test cases test the capability of the non-hydrostatic model to resolve 3D dam-break waves. In all of the test cases, the non-hydrostatic results are compared with experimental data and moreover the quasi-3D SWM results are also provided for comparison. The quasi-3D SWM is reduced from the present non-hydrostatic model as described in the above section. All computations are carried out on a notebook computer with an Intel^(R) Core^(TM) i9–9900K central processing unit (CPU).

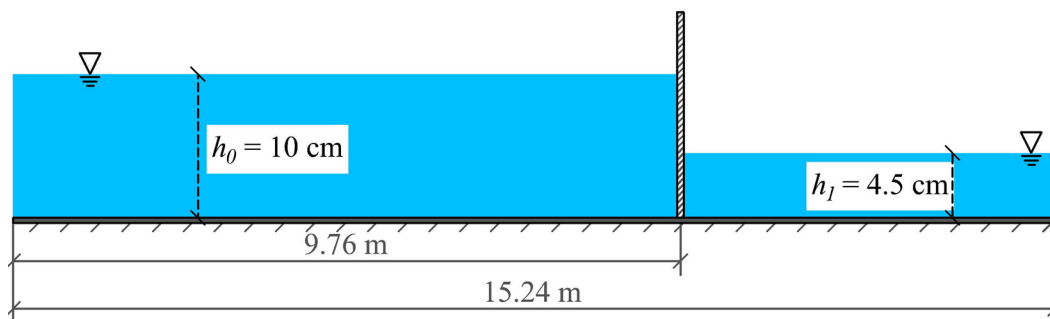


FIG. 4. Schematic sketch of the experiment conducted by Stansby et al. (1998).

The CPU is an eight-core processor with sixteen threads, a base frequency of 3.6 GHz and a peak frequency of 5.0 GHz. The proposed non-hydrostatic model was implemented based on C# parallel class, which provides library-based data parallel replacements for loops. Both the non-hydrostatic model results and the quasi-3D SWM results are obtained by using five horizontal layers in the vertical direction. Notably, after mesh sensitivity analysis, neither model results can be improved by increasing the number of horizontal layers for any of the test cases.

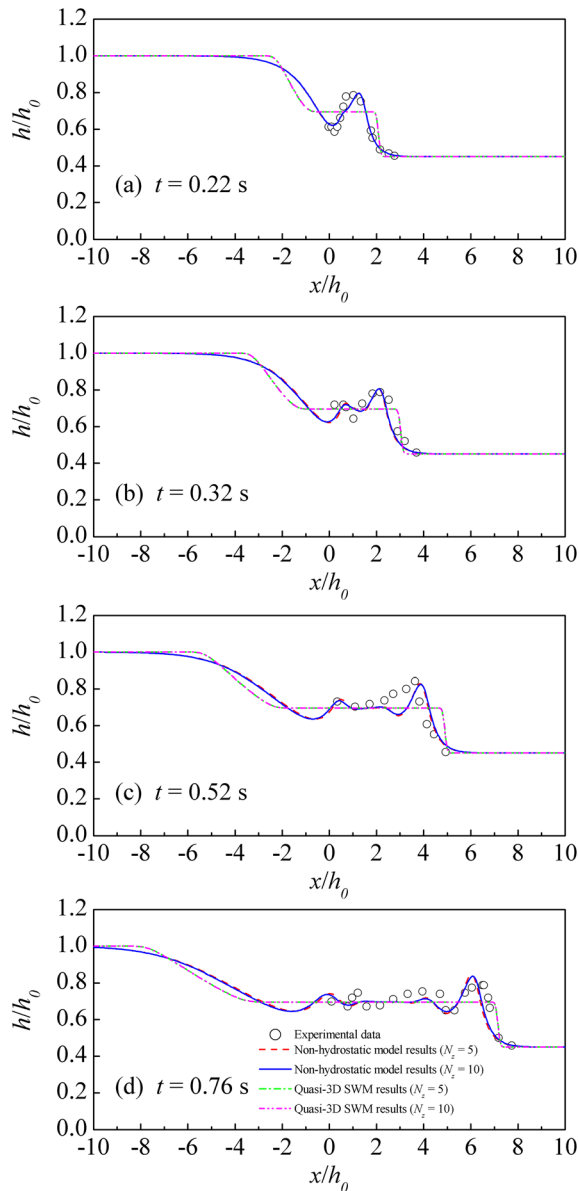


FIG. 5. Comparisons of the free-surface profile between the quasi-3D SWM results, the non-hydrostatic model results, and experimental data at (a) $t = 0.22$ s, (b) $t = 0.32$ s, (c) $t = 0.52$ s, and (d) $t = 0.76$ s.

A. Initial stages of dam-break flow

Many research studies (Cantero-Chinchilla *et al.*, 2016; Ozmen-Cagatay and Kocaman, 2010; and Shigematsu *et al.*, 2004) have shown that the non-hydrostatic effect plays an important role in the initial stages of dam-break flows and that 2D SWMs cannot predict this process accurately. Stansby *et al.* (1998) experimentally investigated the initial stages of dam-break flow in a horizontal channel of a rectangular section. Experimental data have been used to validate numerical models, including VOF models (Marsooli and Wu, 2014 and Shigematsu *et al.*, 2004) and the Boussinesq-type model (Cantero-Chinchilla *et al.*, 2016). In this study, we will present that the developed non-hydrostatic model can also accurately resolve the initial stage of dam-break flows.

As shown in Fig. 4, the experiment of Stansby *et al.* (1998) was carried out in a flume 15.24 m long, 0.4 m wide, and 0.4 m high. Both

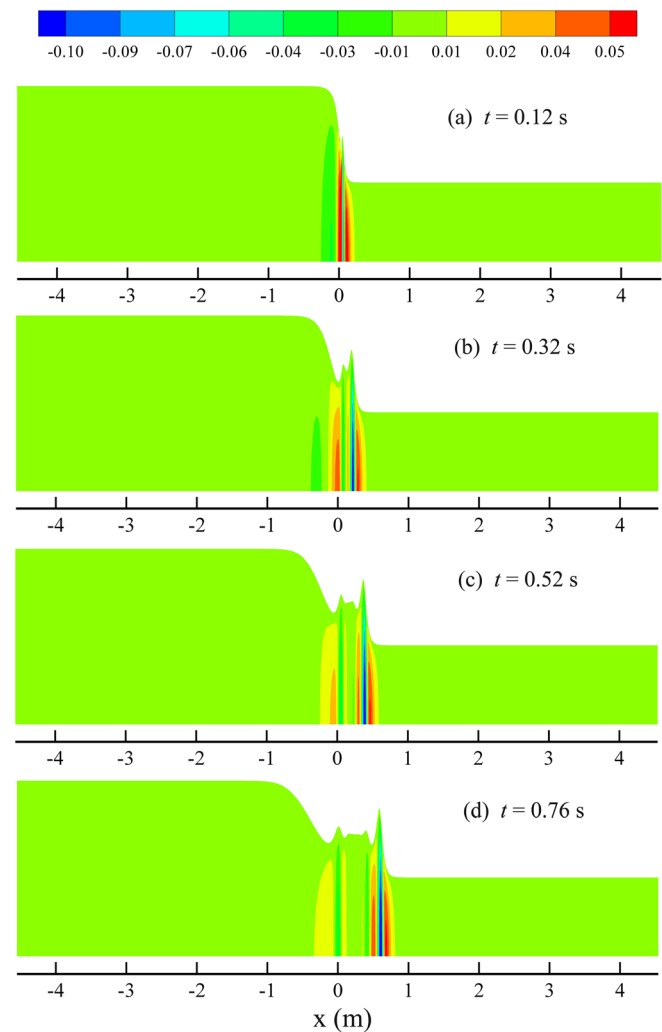


FIG. 6. The normalized non-hydrostatic pressure field q (m^2/s^2) at (a) $t = 0.12$ s, (b) $t = 0.32$ s, (c) $t = 0.52$ s, and (d) $t = 0.76$ s. (The vertical scale has been amplified by a factor of 25.)

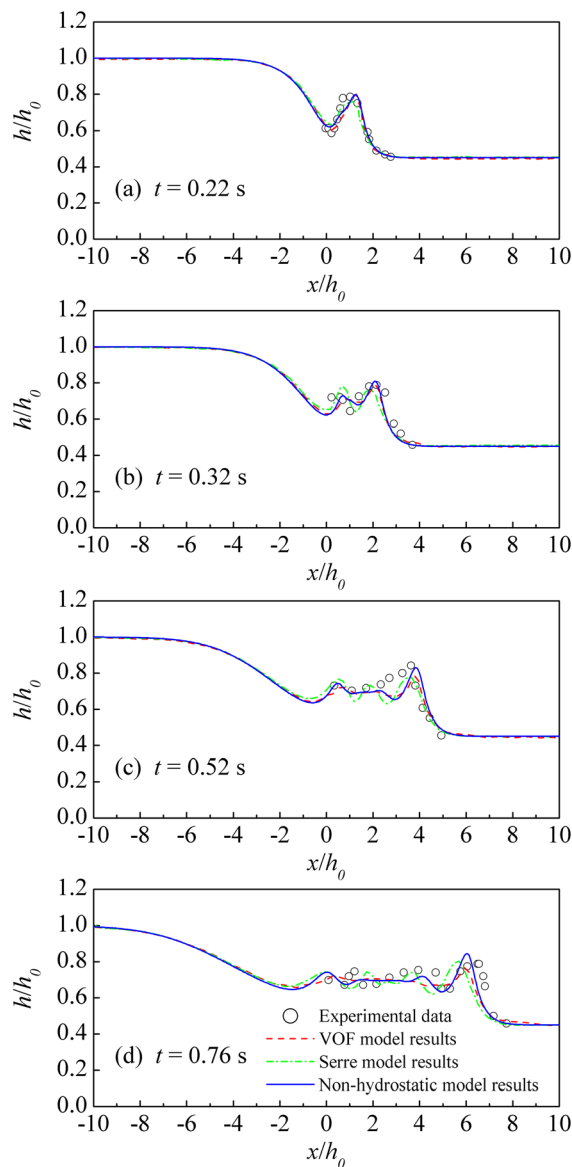


FIG. 7. Comparisons of the free-surface profile between the VOF model results, the Serre model results, the non-hydrostatic model results, and experimental data at (a) $t = 0.22$ s, (b) $t = 0.32$ s, (c) $t = 0.52$ s, and (d) $t = 0.76$ s.

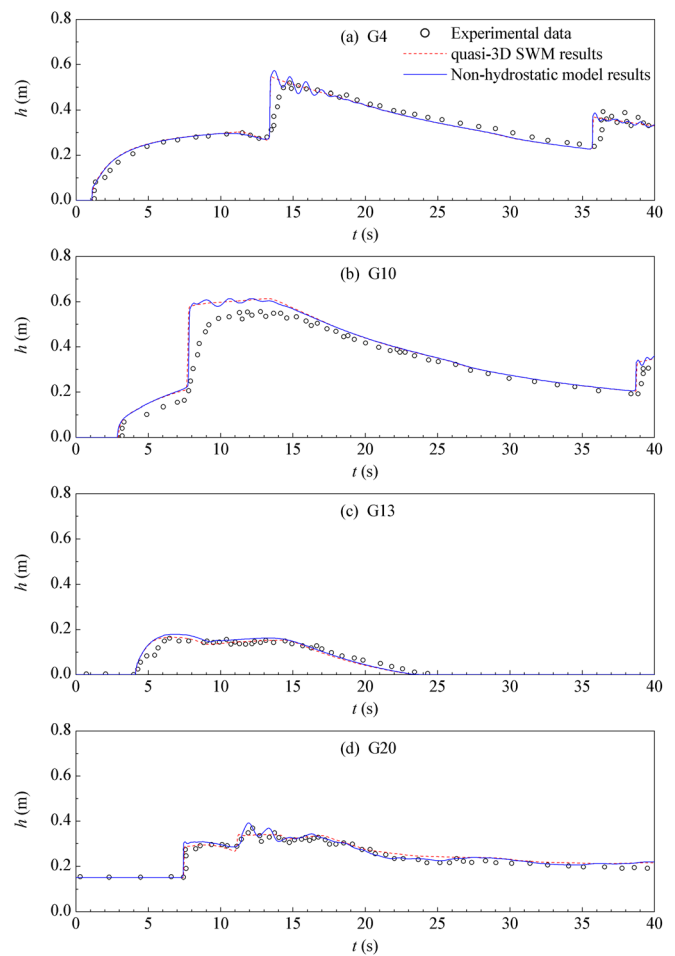


FIG. 9. Comparisons of the time histories of the water depth at four gauging points between the quasi-3D SWM results, the non-hydrostatic model results and experimental data. (a) Location G4, (b) Location G10, (c) Location G13, and (d) Location G20.

ends of the flume were closed, and the dam was located 9.76 m downstream of the upper end. This computation was conducted on a horizontal triangular mesh with an average grid size of 0.6 cm. The time step was set to 0.001 s. The roughness value k_s was taken as 2.0×10^{-4} .

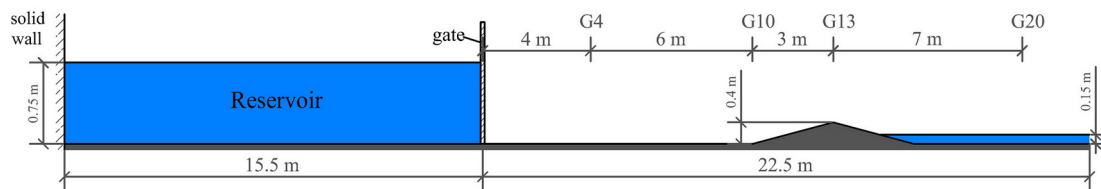


FIG. 8. Schematic sketch of dam-break flows over a triangular bottom sill.

Figure 5 shows comparisons of the free-surface profile between the quasi-3D SWM results, the non-hydrostatic model results, and the experimental data. The spatial scales are normalized by the upstream water depth h_0 and $x/h_0 = 0$ is the dam location. Both model results with $N_z = 5$ and 10 were provided for comparison. Both model results with five horizontal layers are rather similar to those with ten horizontal layers, indicating grid convergence when $N_z \geq 5$. The non-hydrostatic model predicts free-surface profiles well, while the quasi-3D SWM shows classical dam-break results, which disagree with the experimental data. This indicates that the non-hydrostatic effect plays a very important role in the initial stage of the dam-break flow. Figure 6 depicts the calculated normalized non-hydrostatic pressure field under the water surface obtained by $N_z = 5$. The non-hydrostatic pressure is very strong in the vicinity of the dam site at time $t = 0.12$ s. At other times, under the leading and larger wave crest, the non-hydrostatic pressure always has a negative value, while stronger and positive pressure can be observed on both sides of the crest.

Figure 7 compares the proposed non-hydrostatic model results with the other two sets of numerical results. The proposed model results were obtained when $N_z = 5$. The VOF model results are obtained from Marsooli and Wu (2014), in which the computational domain is discretized by a grid spacing of 0.5 cm. The Serre model (Cantero-Chinchilla *et al.*, 2016) solves the depth-averaged conservation of mass and momentum equations (Castro-Orgaz *et al.*, 2015) and incorporates a wave breaking model (Hosoda and Tada, 1994). The horizontal grid size used in the Serre model is 0.75 cm. All of the numerical models predict reasonable results, when compared with the experimental data. However, the overall free-surface profiles captured by the present model are close to those captured by the VOF model. Both the present model and the VOF model behave better than the Serre model. However, the present model predicts larger leading wave crests than the VOF model at $t = 0.32, 0.52$, and 0.76 s.

B. Dam-break flow over a triangular bottom sill

To assess the ability of numerical models to handle flood propagation over uneven dry beds, the Concerted Action on Dam-break Modeling project (CADAM) (Soares-Frazão *et al.*, 2000) and the Investigation of Extreme Flood Processes & Uncertainty project (IMPACT, 2004) have separately conducted a series of experiments on dam-break flows over a triangular bottom sill. In this study, we used the test case selected from the CADAM project to validate the developed non-hydrostatic model.

Within the frame of the CADAM project, a series of large-scale experiments of dam-break flows over a triangular bottom sill were carried out. As illustrated in Fig. 8, the experimental setup combined a reservoir connected to a rectangular channel. The length of the channel was 22.5 m, and the initial water depth in the 15.5 m long upstream reservoir was 0.75 m. A symmetric triangular bottom sill of 0.4 m height and 6 m length was located 13 m downstream of the gate. The channel was dry upstream of the sill, but the water depth was initially set to 0.15 m downstream of it. The upstream boundary was a solid wall, and an open outlet boundary was specified at the downstream end. In this computation, a horizontal triangular mesh with an average grid size of 0.02 m is used to discretize the computational domain. The time step is chosen to be 0.0016 s. The roughness value k_s is also set to 2.0×10^{-4} . In this example, to handle wave breaking, a special numerical technique is necessary for the non-hydrostatic model.

The following relationship presented by Kennedy *et al.* (2000) is incorporated in the present model to detect the beginning of a breaking event:

$$\partial\eta/\partial t \geq \alpha\sqrt{gh}, \quad (31)$$

where $\alpha = 0.1$ is taken as a constant value in this study.

Equation (31) indicates that wave breaking occurs when $\partial\eta/\partial t$ is larger than a specified limit value. After a wave breaks, the hydrostatic pressure distribution is assumed at the breaking location. This wave breaking model has been successfully implemented by nearshore wave models (Shirkavand and Badiei, 2014 and Tonelli and Petti, 2010).

Figure 9 shows comparisons of the time histories of the water depth at four gauging points between the two sets of numerical results and experimental data. At the former three gauging points G4, G10, and G13, the non-hydrostatic model results are in general good agreement with the quasi-3D SWM results, except that the non-hydrostatic model predicts undular water surfaces near the front of the bore at the gauging points G4 and G10. At gauging point G20, very good results are obtained with the non-hydrostatic model, which reproduces the oscillating behavior of the measurement. Based on the present results and the published results obtained from 2D SWMs (Chang *et al.*, 2011 and Kao and Chang, 2012), we can conclude that the non-hydrostatic effect plays an important role behind the sill in this example, where models with the hydrostatic assumption cannot predict accurate results.

C. 3D partial dam-break flow

This example considers the 3D partial dam-break flow experiment carried out by Fraccarollo and Toro (1995). As shown in Fig. 10, the laboratory setup consists of a reservoir connected to a rectangular channel by a partially broken dam. The reservoir is 2 m wide and 1 m long with an initial water depth of $h_0 = 0.6$ m. The rectangular channel is dry with an open outlet and side boundaries. Data are measured at seven gauging points to validate the present model. This test case has been successfully simulated by the VOF-based model developed by Marsooli and Wu (2014) and a 3D model (Ferrari *et al.*, 2010), which utilized a smooth particle hydrodynamics method to solve the weakly compressible NSE.

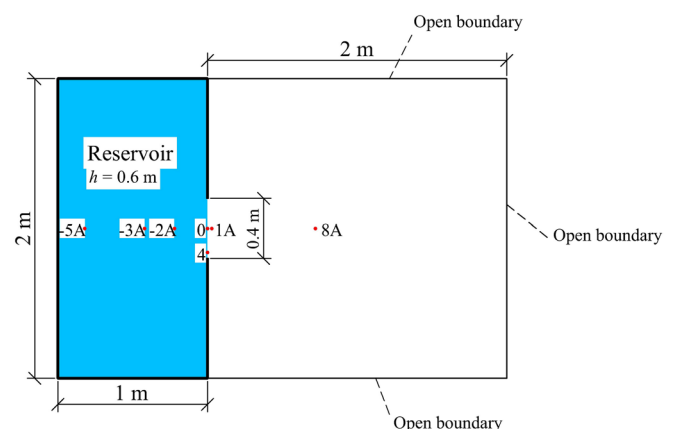


FIG. 10. Schematic sketch of the partial dam-break flow experiment.

In this computation, the computational domain is discretized by a horizontal mesh comprising a total of 16 665 triangles. The smallest horizontal grid size is near the broken dam and is 0.02 m. The time step is taken as 0.001 s, and the total simulation time is 10 s. The roughness value k_s is chosen as 8.0×10^{-3} . The total CPU time for the non-hydrostatic model is approximately 0.18 h.

Comparisons of the time histories of the water depth at gauging points between the two sets of numerical results and experimental data are shown in Fig. 11. The quasi-3D SWM predicts an oscillating water surface during the first 4 s, which deviates from the experimental data, while the non-hydrostatic results show a better agreement with the measured data. Figure 12 depicts comparisons of the time histories

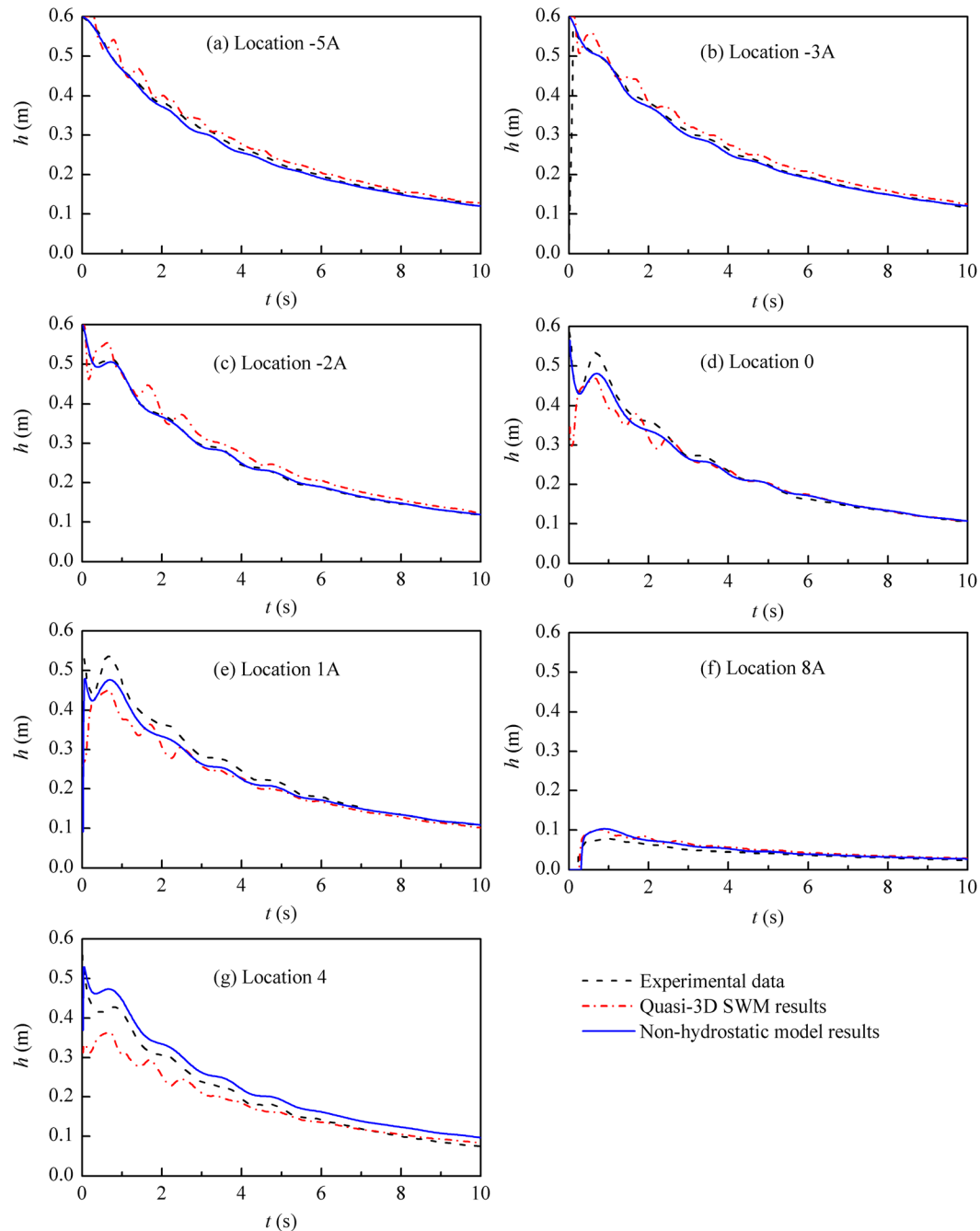


FIG. 11. Comparisons of the time histories of the water depth at gauging points between the quasi-3D SWM results, the non-hydrostatic model results and experimental data. (a) Location -5A, (b) Location -3A, (c) Location -2A, (d) Location 0, (e) Location 1A, (f) Location 8A, and (g) Location 4.

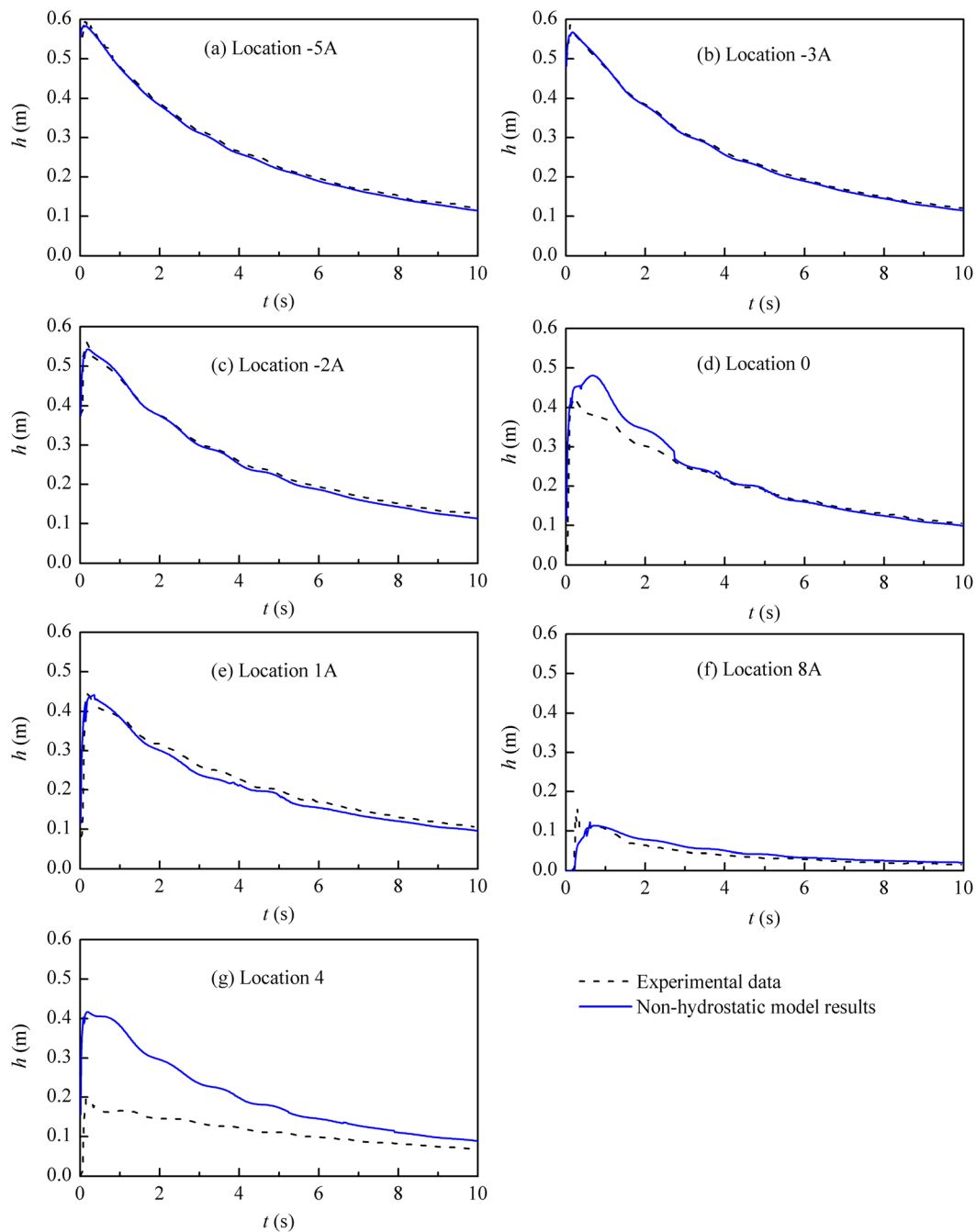


FIG. 12. Comparisons of the time histories of the bottom pressure at gauging points between the non-hydrostatic model results and experimental data. (a) Location -5A, (b) Location -3A, (c) Location -2A, (d) Location 0, (e) Location 1A, (f) Location 8A, and (g) Location 4.

of the bottom pressure at gauging points between the non-hydrostatic model results and experimental data. The non-hydrostatic model predicts larger bottom pressures at gauging points 0 and 4. However, at the other gauging points, the agreement between the present model results and experimental data is quite good. Figure 13 shows the

comparisons of the time histories of the velocity in the longitudinal direction at two gauging points between the two sets of numerical results and the experimental data. Overall, the non-hydrostatic model behaves better than the quasi-3D SWM and reproduces the longitudinal velocity fairly well when compared with the experimental data.

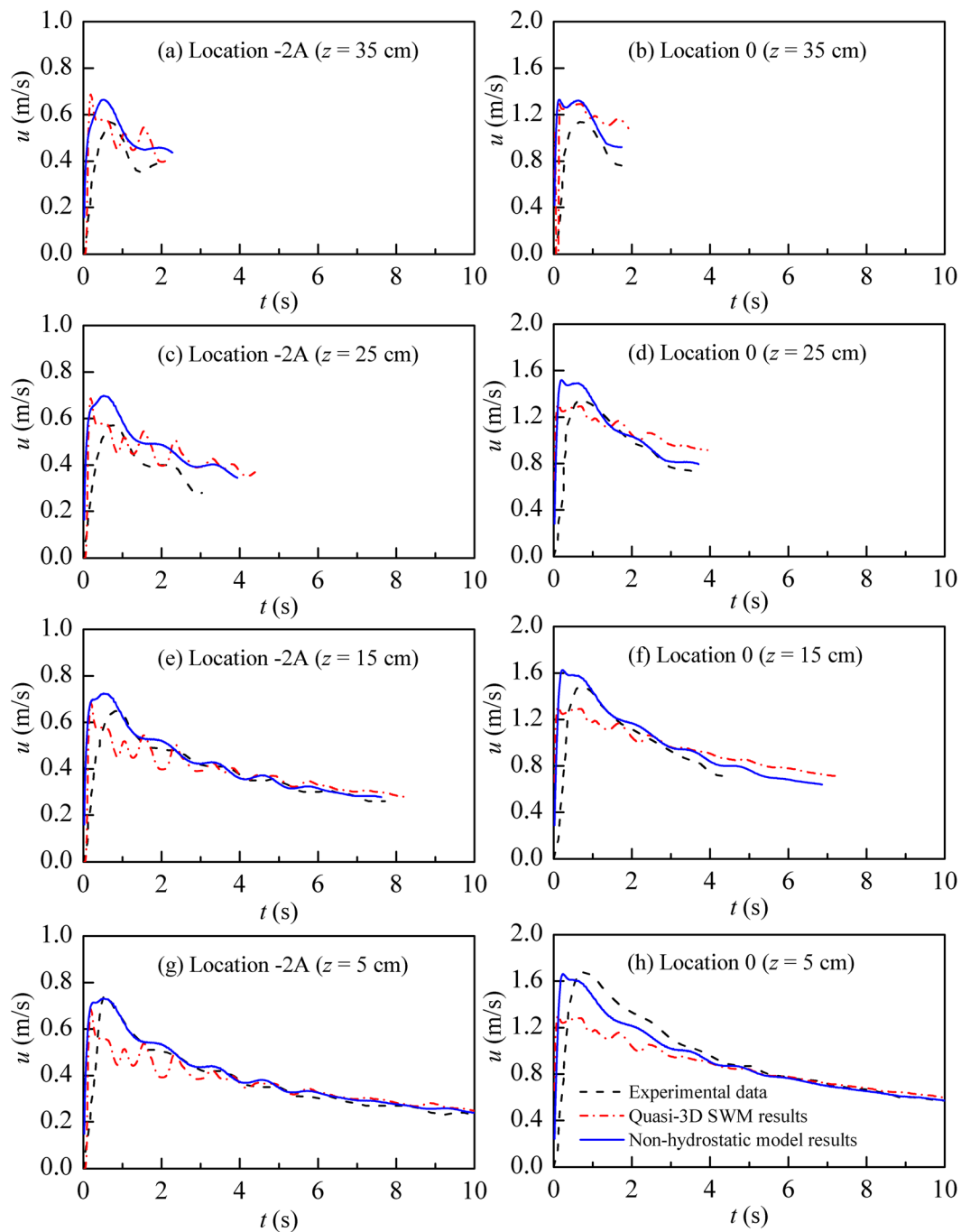


FIG. 13. Comparisons of the time histories of the velocity in the longitudinal direction at two gauging points between the quasi-3D SWM results, the non-hydrostatic model results, and experimental data. (a) Location $-2A$ ($z = 35$ cm), (b) Location 0 ($z = 35$ cm), (c) Location $-2A$ ($z = 25$ cm), (d) Location 0 ($z = 25$ cm), (e) Location $-2A$ ($z = 15$ cm), (f) Location 0 ($z = 15$ cm), (g) Location $-2A$ ($z = 5$ cm), and (h) Location 0 ($z = 5$ cm).

D. Dam-break flow in a 45° bend channel

A dam-break flow in a bend channel with a complicated flow structure has been widely used for validation of numerical models. As illustrated by previous experiments (Soares-Frazão *et al.*, 2000 and

Soares-Frazão and Zech, 2002) and numerical models (Kao and Chang, 2012; Kim and Lynett, 2011; Lai *et al.*, 2005; and Ortiz, 2014), when a dam-break flow encounters a channel bend, part of the flow is reflected, which results in a bore receding into the upstream reservoir

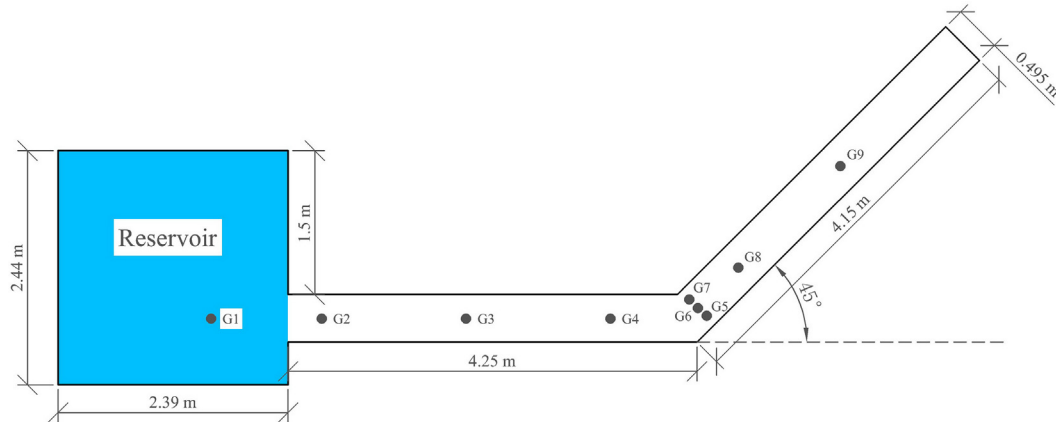


FIG. 14. Schematic sketch of the dam-break flow in a 45° bend channel.

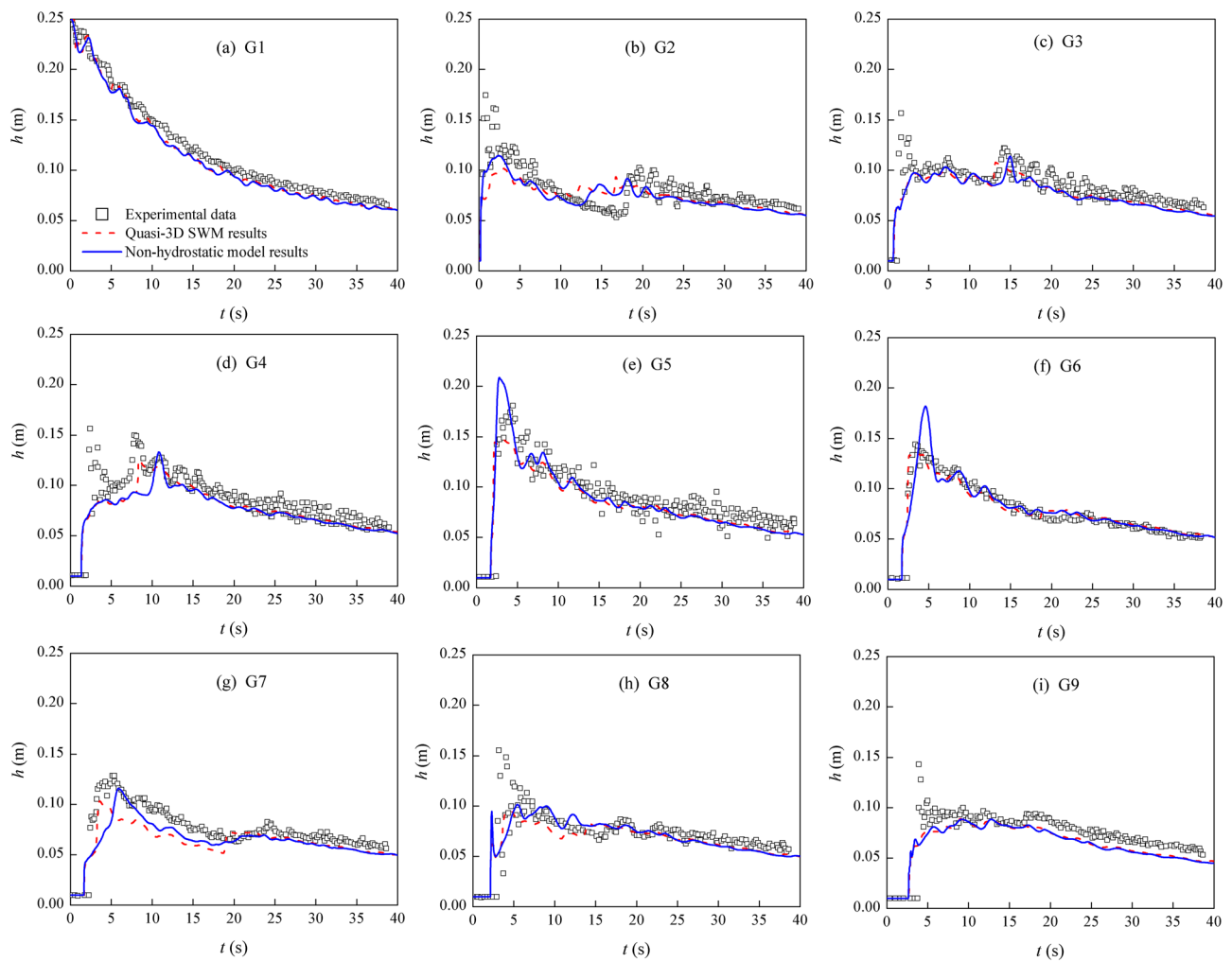


FIG. 15. Comparisons of the time histories of the water depth at gauging points between the quasi-3D SWM results, the non-hydrostatic model results and experimental data. (a) Location G1, (b) Location G2, (c) Location G3, (d) Location G4, (e) Location G5, (f) Location G6, (g) Location G7, (h) Location G8, and (i) Location G9.

and the passing water in the downstream direction flows with multiple smaller reflections against the channel wall. In this study, we will perform a simulation on the experiment of a dam-break flow in a 45° bend channel (Soares-Frazão *et al.*, 2000). Figure 14 shows a sketch of the geometry and the size of the experiment. Nine gauging points are used to measure the time histories of the water depth. Both the reservoir and the channel are horizontal. Initially, the water depths are 0.25 m in the reservoir and 0.01 m in the channel. All of the boundaries are solid walls, except at the end of the channel, which is an open boundary.

In the computation, we use a horizontal mesh comprising a total of 31 214 triangles to cover the computational domain. The average grid sizes are 0.05 m in the reservoir and 0.02 m in the channel. The time step is taken as 0.0008 s, and the total simulation time is 40 s. The roughness value k_s is taken as 5.0×10^{-3} . The total CPU time for the non-hydrostatic model is approximately 1.87 h.

The comparisons of the time histories of the water depth at gauging points between the two sets of numerical results and experimental data are displayed in Fig. 15. Overall, both numerical results are in generally good agreement with the experimental data. However, the non-hydrostatic model captures the oscillating behavior of the reflections from the bend, while the quasi-3D SWM predicts relatively smoother solutions. As a result, the maximum water depth simulated by the non-hydrostatic model is greater than that predicted by the quasi-3D SWM at gauging points G2–G8. This indicates that dam-break flow risk may be underestimated by SWMs.

E. Flash flood flows in a simplified urban district

Within the framework of the IMPACT project (IMPACT, 2014), Testa *et al.* (2007) performed a series of experiments on the flooding of an urban district model, which has been widely used for testing 2D SWMs (Dottori and Todini, 2013; Jeong *et al.*, 2012; and Kim *et al.*, 2014). The experiments were performed on a reduced physical model (scale 1:100) of the Toce River valley, in which flood propagation experiments within the CADAM project (Soares-Frazão *et al.*, 2000) were conducted and were studied by numerical models, including the VOF-based model (Marsooli and Wu, 2014) and 2D SWMs (Chang *et al.*, 2011 and Kao and Chang, 2012). There are two different layouts of the city model considered in the experiments. One is called aligned, in which buildings are placed in rows approximately parallel to the main axis of the valley, while in the other layout buildings are placed in a staggered manner. In this final example, flood propagation experiments on the aligned city layout are used to further test the developed non-hydrostatic model.

The physical model, along with its topography and position of gauging points, is shown in Fig. 16. More details can be found in Testa *et al.* (2007). The domain is initially dry. As shown in Fig. 17, two different inflow hydrographs called low and high are specified at the upstream boundary. At the downstream end of the domain, the open boundary condition is specified. In this computation, the horizontal domain is discretized by 20 820 triangles with grid sizes varying between 0.1 and 0.03 m. As a result, the total number of 3D grids is 104 100. The time step is set to 0.0025 s, and the total simulation time is 60 s. The roughness value k_s is set to 5.0×10^{-3} . For the non-hydrostatic model, the CPU times are 0.40 and 0.49 h for the low- and high-inflow hydrographs, respectively. Notably, Marsooli and Wu (2014) employed their VOF model to simulate a similar test case on

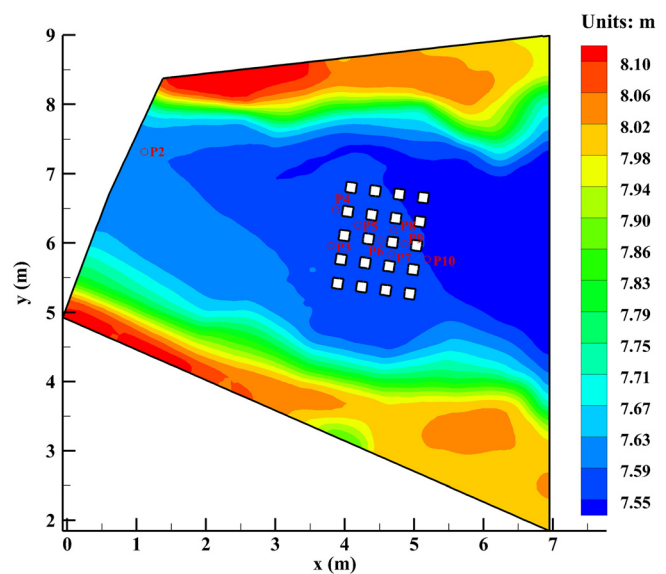


FIG. 16. The physical model with the topography and the position of gauging points. Buildings are represented by the squares.

an Intel Core i7 processor with a base frequency of 3.2 GHz, but they used approximately 3 100 000 grids to cover the computational domain. Their model was run on a single CPU core, and the CPU time was approximately 205 h for a 180 s simulation.

Figures 18 and 19 show the time histories of the water depth at different gauging points for the low- and high-inflow hydrographs, respectively. The overall agreement between the two model results and the measured data is acceptable. The non-hydrostatic model results are quite similar to the quasi-3D SWM results for both the low- and high-inflow hydrographs. However, for the low-inflow hydrograph, the non-hydrostatic model captures the water depth with reflected waves at gauging points P3 and P4.

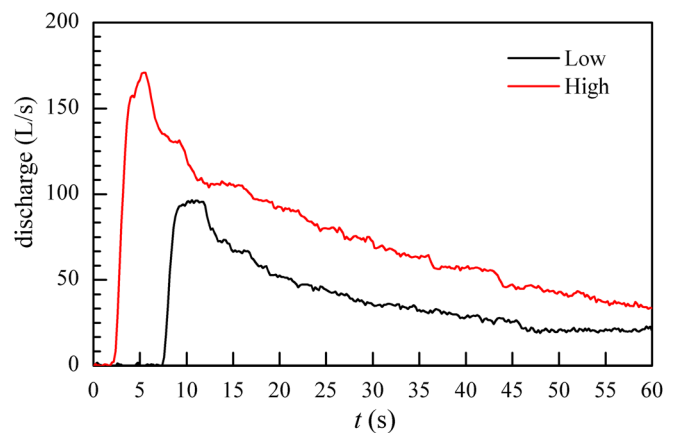


FIG. 17. The two inflow hydrographs.

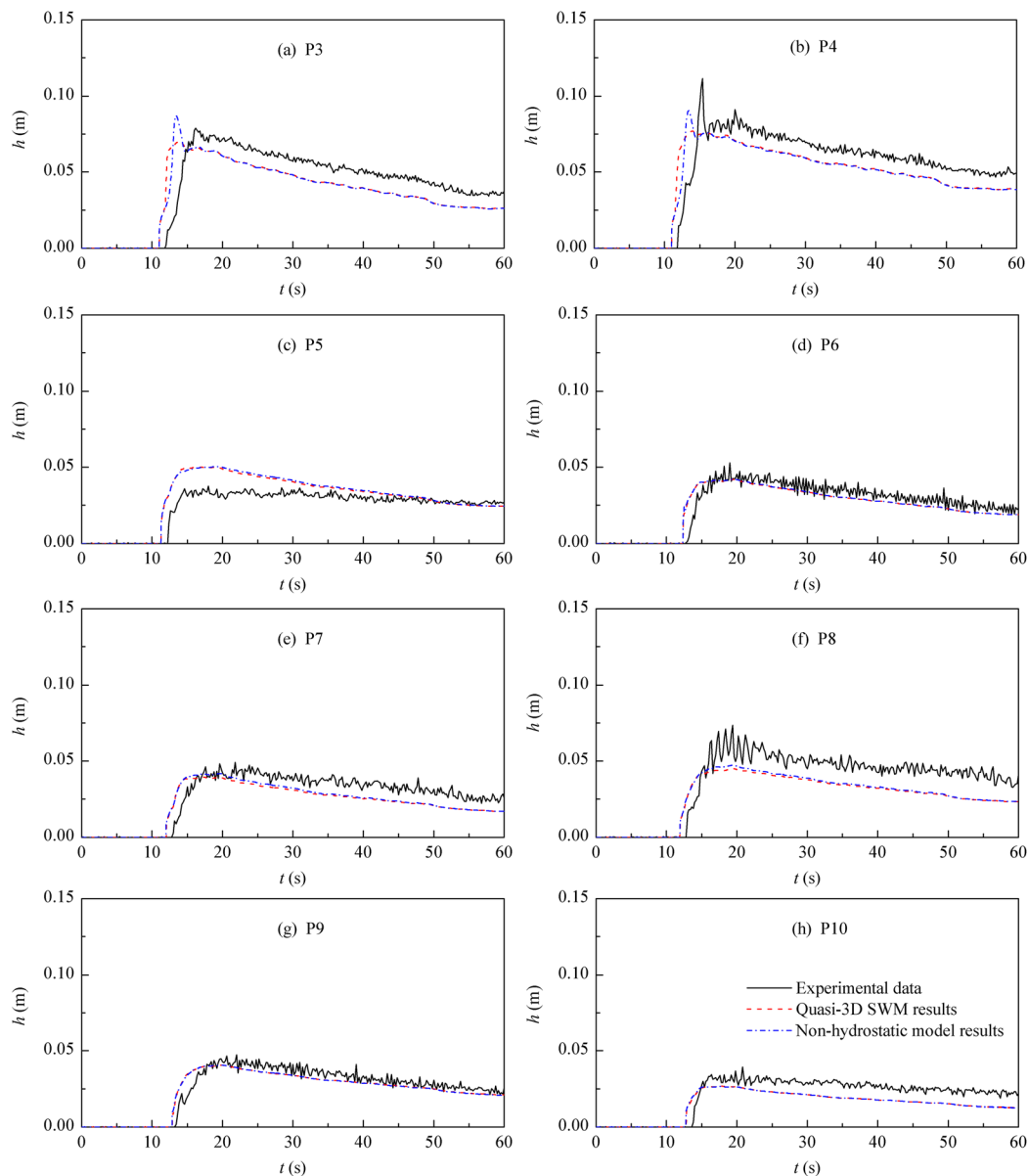


FIG. 18. Comparisons of the time histories of the water depth at gauging points between the quasi-3D SWM results, the non-hydrostatic model results and experimental data for the low-inflow hydrograph. (a) Location P3, (b) Location P4, (c) Location P5, (d) Location P6, (e) Location P7, (f) Location P8, (g) Location P9, and (h) Location P10.

V. CONCLUSIONS

This paper presents a 3D non-hydrostatic model to predict dam-break flows. The model solves the RANS equations with the projection method and makes use of a boundary-fitted coordinate system in the vertical direction. Eddy viscosity approximations are incorporated into the model. The governing equations are discretized by a combination of finite difference and finite volume methods in a 3D grid system, which is unstructured in the horizontal plane, but structured in the vertical direction. Based on the horizontal unstructured grids, Perot's scheme is used to achieve a conservative advection scheme for the momentum equation.

In all test cases, the non-hydrostatic model results were compared with experimental data and showed generally good agreement by using five horizontal layers in the vertical discretization. This indicates that the developed model can accurately consider non-hydrostatic effects using a relatively coarse vertical discretization. Moreover, it can reasonably handle 2D and 3D dam-break flows over flat and uneven bottoms with complex geometries.

To better evaluate the proposed non-hydrostatic model, a quasi-3D SWM reduced from the non-hydrostatic model is also employed to predict all the examples. Comparisons of the two model results have

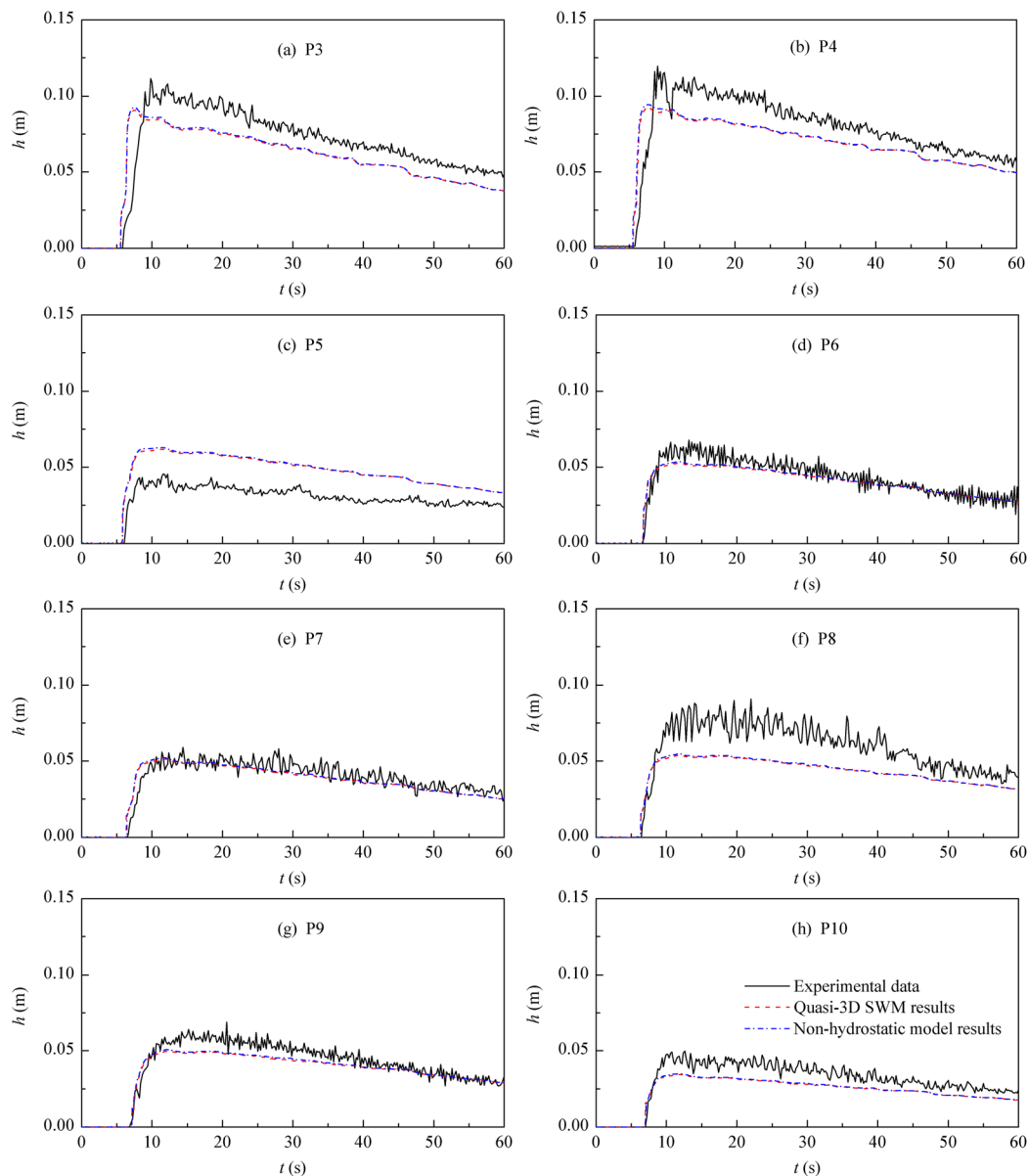


FIG. 19. Comparisons of time histories of the water depth at gauging points between the quasi-3D SWM results, the non-hydrostatic model results and experimental data for the high-inflow hydrograph. (a) Location P3, (b) Location P4, (c) Location P5, (d) Location P6, (e) Location P7, (f) Location P8, (g) Location P9, and (h) Location P10.

shown that non-hydrostatic effects play a certain role in the first four test cases. In summary, the proposed non-hydrostatic model can predict dam-break flows involving non-hydrostatic effects and can be viewed as an attractive alternative to simulating 3D dam-break flows.

ACKNOWLEDGMENTS

This research was supported by the National Natural Science Foundation of China (Grant Nos. 52171248, 51720105010, and 51979029), LiaoNing Revitalization Talents Program (Grant No.

XLYC1807010), and the Fundamental Research Funds for the Central Universities (Grant Nos. DUT2019TB02 and DUT21LK01).

AUTHOR DECLARATIONS

Conflict of Interest

The authors have no conflicts to disclose.

DATA AVAILABILITY

The data that support the findings of this study are available from the corresponding author upon reasonable request.

REFERENCES

- Ai, C. and Ding, W., "A 3D unstructured non-hydrostatic ocean model for internal waves," *Ocean Dyn.* **66**, 1253–1270 (2016).
- Ai, C. and Jin, S., "Non-hydrostatic finite volume model for non-linear waves interacting with structures," *Comput. Fluids* **39**, 2090–2100 (2010).
- Ai, C. and Jin, S., "A multi-layer non-hydrostatic model for wave breaking and run-up," *Coastal Eng.* **62**, 1–8 (2012).
- Ai, C., Jin, S., and Lv, B., "A new fully non-hydrostatic 3D free surface flow model for water wave motions," *Int. J. Numer. Methods Fluids* **66**, 1354–1370 (2011).
- Ai, C., Ma, Y., Yuan, C., and Dong, G., "Development and assessment of semi-implicit nonhydrostatic models for surface water waves," *Ocean Modell.* **144**, 101489 (2019a).
- Ai, C., Ma, Y., Yuan, C., and Dong, G., "A 3D non-hydrostatic model for wave interactions with structures using immersed boundary method," *Comput. Fluids* **186**, 24–37 (2019b).
- Ai, C., Ma, Y., Yuan, C., and Dong, G., "Non-hydrostatic model for internal wave generations and propagations using immersed boundary method," *Ocean Eng.* **225**, 108801 (2021a).
- Ai, C., Ma, Y., Yuan, C., Xie, Z., and Dong, G., "A three-dimensional non-hydrostatic model for tsunami waves generated by submarine landslides," *Appl. Math. Modell.* **96**, 1–19 (2021b).
- Aricò, C. and Re, L. C., "A non-hydrostatic pressure distribution solver for the nonlinear shallow water equations over irregular topography," *Adv. Water Resour.* **98**, 47–69 (2016).
- Aureli, F., Maranzoni, A., Mignosa, P., and Ziveri, C., "Dam-break flows: Acquisition of experimental data through an imaging technique and 2D numerical modeling," *J. Hydraul. Eng.* **134**(8), 1089–1101 (2008).
- Biscarini, C., Francesco, S. D., and Manciola, P., "CFD modeling approach for dam break flow studies," *Hydrol. Earth Syst. Sci.* **14**, 705–718 (2010).
- Bristeau, M. O., Goutal, N., and Sainte-Marie, J., "Numerical simulations of a non-hydrostatic shallow water model," *Comput. Fluids* **47**, 51–64 (2011).
- Brufau, P., Vazquez-Cendon, M. E., and Garcia-Navarro, P., "A numerical model for the flooding and drying of irregular domains," *Int. J. Numer. Methods Fluids* **39**, 247–275 (2002).
- Cantero-Chinchilla, F. N., Castro-Orgaz, O., Dey, S., and Ayuso, J. L., "Nonhydrostatic dam break Flows. I: Physical equations and numerical schemes," *J. Hydraul. Eng.* **142**(12), 04016068 (2016).
- Castro-Orgaz, O., Hutter, K., Giraldez, J. V., and Hager, W. H., "Nonhydrostatic granular flow over 3D terrain: New Boussinesq-type gravity waves?," *J. Geophys. Res.: Earth Surf.* **120**(1), 1–28, <https://doi.org/10.1002/2014JF003279> (2015).
- Casulli, V. and Zanolli, P., "Semi-implicit numerical modeling of nonhydrostatic free-surface flows for environmental problems," *Math. Comput. Modell.* **36**, 1131–1149 (2002).
- Chang, T. J., Chang, K. H., and Kao, H. M., "A new approach to model weakly nonhydrostatic shallow water flows in open channels with smoothed particle hydrodynamics," *J. Hydrol.* **519**, 1010–1019 (2014).
- Chang, T. J., Kao, H. M., Chang, K. H., and Hsu, M. H., "Numerical simulation of shallow-water dam break flows in open channels using smoothed particle hydrodynamics," *J. Hydrol.* **408**, 78–90 (2011).
- Dottori, F. and Todini, E., "Testing a simple 2D hydraulic model in an urban flood experiment," *Hydrol. Processes* **27**, 1301–1320 (2013).
- Duy, T.-N., Nguyen, V.-T., Phan, T.-H., and Park, W.-G., "An enhancement of coupling method for interface computations in incompressible two-phase flows," *Comput. Fluids* **214**, 104763 (2021).
- Ferrari, A., Fraccarollo, L., Dumbser, M., Toro, E. F., and Armanini, A., "Three-dimensional flow evolution after a dam break," *J. Fluid Mech.* **663**, 456–477 (2010).
- Fraccarollo, L. and Toro, E. F., "Experimental and numerical assessment of the shallow water model for two-dimensional dam-break type problems," *J. Hydraul. Res.* **33**(6), 843–864 (1995).
- Fyhn, E. H., Lervåg, K. Y., Ervik, Å., and Wilhelmsen, Ø., "A consistent reduction of the two-layer shallow-water equations to an accurate one-layer spreading model," *Phys. Fluids* **31**, 122103 (2019).
- Hirt, C. W. and Nichols, B. D., "Volume of fluid (VOF) method for the dynamic of free boundaries," *J. Comput. Phys.* **39**, 201–255 (1981).
- Hosoda, T. and Tada, A., "Free surface profile analysis on open channel flow by means of 1D basic equations with effect of vertical acceleration," *JSE Annu. J. Hydraul. Eng.* **38**, 457–462 (1994) (in Japanese).
- Ii, S., Xie, B., and Xiao, F., "An interface capturing method with a continuous function: The THINC method on unstructured triangular and tetrahedral meshes," *J. Comput. Phys.* **259**, 260–269 (2014).
- IMPACT, 2004, see www.impact-project.net.
- Jeong, W., Yoon, J. S., and Cho, Y. S., "Numerical study on effects of building groups on dam-break flow in urban areas," *J. Hydro-environ. Res.* **6**, 91–99 (2012).
- Kao, H. M. and Chang, T. J., "Numerical modeling of dambreak-induced flood and inundation using smoothed particle hydrodynamics," *J. Hydrol.* **448**, 232–244 (2012).
- Kennedy, A. B., Chen, Q., Kirby, J. T., and Dalrymple, R. A., "Boussinesq modeling of wave transformation, breaking, and runup. I: 1D," *J. Waterw., Port, Coastal, Ocean Eng.* **126**, 39–47 (2000).
- Khankandi, A. F., Tahershamsi, A., and Soares-Frazão, S., "Experimental investigation of reservoir geometry effect on dam-break flow," *J. Hydraul. Res.* **50**(4), 376–387 (2012).
- Kim, B., Sanders, B. F., Schubert, J. E., and Famiglietti, J. S., "Mesh type tradeoffs in 2D hydrodynamic modeling of flooding with a Godunov-based flow solver," *Adv. Water Resour.* **68**, 42–61 (2014).
- Kim, D. H. and Lynett, P. J., "Dispersive and nonhydrostatic pressure effects at the front of surge," *J. Hydraul. Eng.* **137**(7), 754–765 (2011).
- Kocaman, S. and Ozmen-Cagatay, H., "The effect of lateral channel contraction on dam break flows: Laboratory experiment," *J. Hydrol.* **432**, 145–153 (2012).
- Kramer, S. C. and Stelling, G. S., "A conservative unstructured scheme for rapidly varied flows," *Int. J. Numer. Methods Fluids* **58**, 183–212 (2008).
- Lai, J. S., Lin, G. F., and Guo, W. D., "An upstream flux-splitting finite-volume scheme for 2D shallow water equations," *Int. J. Numer. Methods Fluids* **48**, 1149–1174 (2005).
- Lai, Z., Chen, C., Cowles, G. W., and Beardsley, R. C., "A nonhydrostatic version of FVCOM: 2. Mechanistic study of tidally generated nonlinear internal waves in Massachusetts Bay," *J. Geophys. Res.* **115**, C12049, <https://doi.org/10.1029/2010JC006331> (2010).
- LaRocque, L. A., Imran, J., and Chaudhry, M. H., "Experimental and numerical investigations of two-dimensional dam-break flows," *J. Hydraul. Eng.* **139**(6), 569–579 (2013).
- Li, Y. L., Ma, C. P., Zhang, X. H., Wang, K. P., and Jiang, D. P., "Three-dimensional numerical simulation of violent free surface deformation based on a coupled level set and volume of fluid method," *Ocean Eng.* **210**, 106794 (2020).
- Ling, K., Zhang, S., Wu, P.-Z., Yang, S.-Y., and Tao, W.-Q., "A coupled volume-of-fluid and level-set method (VOSET) for capturing interface of two-phase flows in arbitrary polygon grid," *Int. J. Heat Mass Transfer* **143**, 118565 (2019).
- Lu, X., Mao, B., Zhang, X., and Ren, S., "Well-balanced and shock-capturing solving of 3D shallow-water equations involving rapid wetting and drying with a local 2D transition approach," *Comput. Methods Appl. Mech. Eng.* **364**, 112897 (2020).
- Ma, G., Farahani, A. A., Kirby, J. T., and Shi, F., "Modeling wave-structure interactions by an immersed boundary method in a σ -coordinate model," *Ocean Eng.* **125**, 238–247 (2016).
- Ma, G., Shi, F., and Kirby, J. T., "Shock-capturing non-hydrostatic model for fully dispersive surface wave processes," *Ocean Modell.* **43**, 22–35 (2012).
- Ma, Y., Yuan, C., Ai, C., and Dong, G., "Comparison between a non-hydrostatic model and OpenFOAM for 2D wave-structure interactions," *Ocean Eng.* **183**, 419–425 (2019).
- Marsoli, R. and Wu, W., "3-D finite-volume model of dam-break flow over uneven beds based on VOF method," *Adv. Water Resour.* **70**, 104–117 (2014).
- Mignot, E. and Cienfuegos, R., "On the application of a Boussinesq model to river flows including shocks," *Coastal Eng.* **56**, 23–31 (2009).
- Mingham, C. G. and Causon, D. M., "High-resolution finite-volume method for shallow water flows," *J. Hydraul. Eng.* **124**(6), 605–614 (1998).
- Mintgen, F. and Manhart, M., "A bi-directional coupling of 2D shallow water and 3D Reynolds-averaged Navier–Stokes models," *J. Hydraul. Res.* **56**(6), 771–785 (2018).

- Mohapatra, P. K. and Chaudhry, M. H., "Numerical solution of Boussinesq equations to simulate dam-break flows," *J. Hydraul. Eng.* **130**(2), 156–159 (2004).
- Munoz, D. H. and Constantinescu, G., "3-D dam break flow simulations in simplified and complex domains," *Adv. Water Resour.* **137**, 103510 (2020).
- O'Donoghue, T., Pokrajac, D., and Hondebrink, L. J., "Laboratory and numerical study of dambreak-generated swash on impermeable slopes," *Coastal Eng.* **57**(5), 513–530 (2010).
- Oishi, Y., Piggott, M. D., Maeda, T., Kramer, S. C., Collins, G. S., Tsushima, H., and Furumura, T., "Three-dimensional tsunami propagation simulations using an unstructured mesh finite element model," *J. Geophys. Res.: Solid Earth* **118**(6), 2998–3018, <https://doi.org/10.1002/jgrb.50225> (2013).
- Ortiz, P., "Shallow water flows over flooding areas by a flux-corrected finite element method," *J. Hydraul. Res.* **52**(2), 241–252 (2014).
- Osher, S. and Sethian, J. A., "Fronts propagating with curvature-dependent speed: Algorithms based on Hamilton–Jacobi formulations," *J. Comput. Phys.* **79**, 12–49 (1988).
- Ozmen-Cagatay, H. and Kocaman, S., "Dam-break flows during initial stage using SWE and RANS approaches," *J. Hydraul. Res.* **48**(5), 603–611 (2010).
- Ozmen-Cagatay, H. and Kocaman, S., "Dam-break flow in the presence of obstacle: Experiment and CFD simulation," *Eng. Appl. Comput. Fluid Mech.* **5**(4), 541–552 (2011).
- Pan, W., Kramer, S. C., Kärnäb, T., and Piggott, M. D., "Comparing non-hydrostatic extensions to a discontinuous finite element coastal ocean model," *Ocean Modell.* **151**, 101634 (2020).
- Perot, B., "Conservation properties of unstructured staggered mesh schemes," *J. Comput. Phys.* **159**, 58–89 (2000).
- Rijnsdorp, D. P. and Zijlema, M., "Simulating waves and their interactions with a restrained ship using a non-hydrostatic wave-flow model," *Coastal Eng.* **114**, 119–136 (2016).
- Rodi, W., *Turbulence Models and Their Applications in Hydraulics*, 2nd ed. (Delft, 1984).
- Shigematsu, T., Liu, P. L.-F., and Oda, K., "Numerical modeling of the initial stages of dam-break waves," *J. Hydraul. Res.* **42**(2), 183–195 (2004).
- Shirkavand, A. and Badiei, P., "The application of a Godunov-type shock capturing scheme for the simulation of waves from deep water up to the swash zone," *Coastal Eng.* **94**, 1–9 (2014).
- Smagorinsky, J., "General circulation experiments with the primitive equations: 1. The basic experiment," *Mon. Weather Rev.* **91**(3), 99–164 (1963).
- Soares-Frazão, S., "Experiments of dam-break wave over a triangular bottom sill," *J. Hydraul. Res.* **45**, 19–26 (2007).
- Soares-Frazão, S., Morris, M., and Zech, Y., "Concerted action on dambreak modelling: Objectives," in *Project Report, Test Cases, Meeting Proceedings*, Université catholique de Louvain, Civil Engineering Department, Hydraulics Division, Louvain-la-Neuve, Belgium, 2000.
- Soares-Frazão, S. and Zech, Y., "Dam break in channels with 90° bend," *J. Hydraul. Eng.* **128**(11), 956–968 (2002).
- Stansby, P. K., Chegini, A., and Barnes, T. C. D., "The initial stages of dam-break flow," *J. Fluid Mech.* **374**, 407–424 (1998).
- Testa, G., Zuccala, D., Alcrud, F., Mulet, J., and Soares-Frazão, S., "Flash flood flow experiment in a simplified urban district," *J. Hydraul. Res.* **45**, 37–44 (2007).
- Tonelli, M. and Petti, M., "Finite volume scheme for the solution of 2D extended Boussinesq equations in the surf zone," *Ocean Eng.* **37**, 567–582 (2010).
- Vasarmidis, P., Stratigaki, V., Suzuki, T., Zijlema, M., and Troch, P., "Internal wave generation in a non-hydrostatic wave model," *Water* **11**(5), 986 (2019).
- Wu, C. H., Young, C. C., Chen, Q., and Lynett, P. J., "Efficient nonhydrostatic modeling of surface waves from deep to shallow water," *J. Waterw., Port, Coastal, Ocean Eng.* **136**(2), 104–118 (2010).
- Xie, B. and Xiao, F., "Toward efficient and accurate interface capturing on arbitrary hybrid unstructured grids: The THINC method with quadratic surface representation and Gaussian quadrature," *J. Comput. Phys.* **349**, 415–440 (2017).
- Xie, Z., Stoesser, T., and Xia, J., "Simulation of three-dimensional free-surface dam-break flows over a cuboid, cylinder, and sphere," *J. Hydraul. Eng.* **147**(9), 06021009 (2021).
- Young, C. C., Wu, C. H., Liu, W., and Kuo, J., "A higher-order non-hydrostatic σ model for simulating non-linear refraction-diffraction of water waves," *Coastal Eng.* **56**, 919–930 (2009).
- Zhao, D. H., Shen, H. W., Tabios, G. Q., Lai, J. S., and Tan, W. Y., "Finite-volume two-dimensional unsteady-flow model for river basins," *J. Hydraul. Eng.* **120**(7), 863–882 (1994).
- Zhao, F., Gan, J., and Xu, K., "The study of shallow water flow with bottom topography by high-order compact gaskinetic scheme on unstructured mesh," *Phys. Fluids* **33**, 083613 (2021).
- Zijlema, M. and Stelling, G. S., "Further experiences with computing non-hydrostatic free-surface flows involving water waves," *Int. J. Numer. Methods Fluids* **48**, 169–197 (2005).